STUDY AND DEVELOPMENT OF LABEL-FREE OPTICAL BIOSENSORS FOR BIOMEDICAL APPLICATIONS

BY

CHARLES J. CHOI

DISSERTATION

Submitted in partial fulfillment of the requirements
for the degree of Doctor of Philosophy in Electrical and Computer Engineering
in the Graduate College of the
University of Illinois at Urbana-Champaign, 2011

Urbana, Illinois

Doctoral Committee:

Professor Brian T. Cunningham, Chair
Professor Rashid Bashir
Professor Paul J. A. Kenis
Assistant Professor Gang L. Liu

ABSTRACT

For the majority of assays currently performed, fluorescent or colorimetric chemical labels are commonly attached to the molecules under study so that they may be readily visualized [1-3]. The methods of using labels to track biomolecular binding events are very sensitive and effective, and are employed as standardized assay protocol across research labs worldwide. However, using labels induces experimental uncertainties due to the effect of the label on molecular conformation, active binding sites, or inability to find an appropriate label that functions equivalently for all molecules in an experiment [4]. Therefore, the ability to perform highly sensitive biochemical detection without the use of fluorescent labels would further simplify assay protocols and would provide quantitative kinetic data, while removing experimental artifacts from fluorescent quenching, shelf-life, and background fluorescence phenomena [5].

In view of the advantages mentioned above, the study and development of optical label-free sensor technologies have been undertaken here. In general, label-free photonic crystal (PC) biosensors and metal nanodome array surface-enhanced Raman scattering (SERS) substrates, both of which are fabricated by nanoreplica molding process, have been used as the method to attack the problem. Chapter 1 shows the work on PC label-free biosensor incorporated microfluidic network for bioassay performance enhancement and kinetic reaction rate constant determination. Chapter 2 describes the work on theoretical and experimental comparison of label-free biosensing in microplate, microfluidic, and spot-based affinity capture assays. Chapter 3 shows the work on integration of PC biosensor with actuate-to-open valve microfluidic chip for pL-volume combinatorial mixing and screening application. In Chapter 4, the development and

characterization of SERS nanodome array is shown. Lastly, Chapter 5 describes SERS nanodome sensor incorporated tubing for point-of-care monitoring of intravenous drugs and metabolites.

ACKNOWLEDGMENTS

I would like to acknowledge my adviser Professor Brian T. Cunningham, without whom this work would not have been possible, for his continuous support, advice, and belief in me. I would also like to acknowledge my colleagues in the Nano Sensors Group for helpful discussions and support. I extend my gratitude to Derek Puff at SRU Biosystems, David Dralle, Brian Bole, and Jonathan Weyhenmeyer for their contributions. Finally, I would like to thank my family and friends for their support and encouragement.

The material in this dissertation is based upon work supported by the National Science Foundation under Award No. DMI 0328162, 0427657, and ECCS 09-24062. I also acknowledge SRU Biosystems for providing financial support for this work, the staff of the Micro and Nanotechnology Laboratory, and the Center for Nanoscale Chemical-Electrical-Mechanical Manufacturing Systems (Nano-CEMMS) at the University of Illinois at Urbana-Champaign.

TABLE OF CONTENTS

CHAPTER 1: LABEL-FREE PHOTONIC CRYSTAL BIOSENSOR INTEGRATED MICROFLUIDIC CHIP FOR DETERMINATION OF KINETIC REACTION RATE CONSTANTS

1.1 Introduction

The ability to perform biochemical and cellular analysis using small reagent volumes and high measurement throughput has been one of the driving forces behind the development of microfluidic lab-on-a-chip (LOC) devices and micro-total-analysis systems (μTAS) [6-8]. Often, such systems are produced using microfabrication methods upon glass or silicon substrates with custom-designed interfaces that allow microliter quantities of reagents to be introduced into a system of microfluidic channels. However, within the field of pharmaceutical discovery and laboratory-based diagnostic assays, a great deal of liquid handling infrastructure currently exists for interfacing with standard 96, 384, and (more recently) 1536-well microplates. For this reason, it is desirable for a label-free biosensing system to easily integrate with these standard formats to enable high throughput in a single-use disposable format. This requirement has driven the commercial adoption of photonic crystal (PC) biosensor microplates for applications in pharmaceutical high throughput screening for measuring protein-protein interactions [9-12], protein-small molecule interactions [13], cell-based assays [14, 15], and cell-drug interactions [16]. While label-free optical biosensors embedded within the bottom surface of microplate wells offer a convenient high throughput detection system, the kinetics that drive detection of biomolecules to attach to the sensor surface is based mainly upon diffusion. Many publications have demonstrated the efficacy of biosensors interfaced with microfluidic channels as a means for obtaining detection kinetics that are

limited by chemical reaction rates. These can serve as a rapid and sensitive means for characterizing ligand-analyte binding affinity constants through the rate of change of detected biosensor signal [17-21].

Recently, the co-fabrication of PC biosensors with a network of microfluidic channels was demonstrated using a silicon "master" template wafer that contains both the micrometer-scale surface structure for microfluidic channels and the nanometer-scale surface features for the PC biosensor structure. The resulting PC sensors and fluid channels were automatically self-aligned, and were fabricated over a 3 × 5 inch area on flexible plastic substrates for integration with a standard 96-well microplate. A simple valveless control scheme was also demonstrated in which some wells were designated as "control" wells. The control wells were used for introducing capture molecules and analytes through the microfluidic channels for real-time monitoring of up to 11 biochemical binding interactions in parallel with a high resolution label-free imaging detection instrument [22]. With the device, reduction in the end-point binding assay time was achieved, but kinetic analysis could not be effectively performed with the use of a long flow channel length (64 mm), which was required to bring analytes from the "analyte" microplate wells to the central measurement point. To ensure equal flow rate for a pneumatic pressure applied equally to all "analyte" wells, serpentine flow paths were implemented for wells with closest proximity to the measurement point. Despite these efforts, the previously reported chip exhibited flow rate differences between analyte flow channels, and limitations on the maximum achievable fluid flow rate.

In this chapter, a PC biosensor integrated microfluidic chip compatible with a 384-well microplate format is demonstrated. The device structure enables low volume

kinetic analysis of protein-protein interactions through 5 analyte flow channels with a single control point and offers higher assay density. It is important to note that the 384-well fluid channel microplate reported in this chapter requires significantly shorter analyte travel distance from the inlet region to the PC detection region, compared to the 96-well microplate sensor format reported previously, in which kinetic analysis could not be performed effectively. This is important especially for accurate kinetic analysis of low analyte concentrations because short analyte travel distance enables very low flow latency and helps mitigate the effects of analyte molecule depletion through attachment to the channel walls before reaching the detection region. The resulting biosensor microfluidic microplate and detection instrument are capable of rapid and high throughput characterization of biochemical binding constants in a format that is compatible with existing 384-well microplate liquid handling systems.

1.2 Materials and Methods

The photonic crystal (PC) shown in Figure 1.1 is a nanostructure comprising a periodically modulated low refractive index UV cured polymer linear periodic grating coated with a high refractive index dielectric layer of titanium dioxide (TiO_2). The device is designed to reflect only a narrow band of wavelengths with 100% efficiency when illuminated with white light at normal incidence [23]. The resonant reflection is due to evanescent diffracted orders coupling to modes of an effective high refractive index layer, which are then re-radiated through diffraction in-phase with the reflected zeroth-order wave [24]. A positive shift of the reflected peak wavelength value (PWV) indicates adsorption of material on the sensor surface. Previously, PC optical biosensors

have been fabricated on continuous sheets of plastic film using a process in which the periodic surface structure is replica molded directly from a silicon master wafer using a UV-cured polymer material [9-12, 14, 15]. The use of a continuous, roll-based, high-throughput replication process enables low-cost mass-production of large surface-area devices for single-use disposable products, capable of integration into microplates and microarray slides.

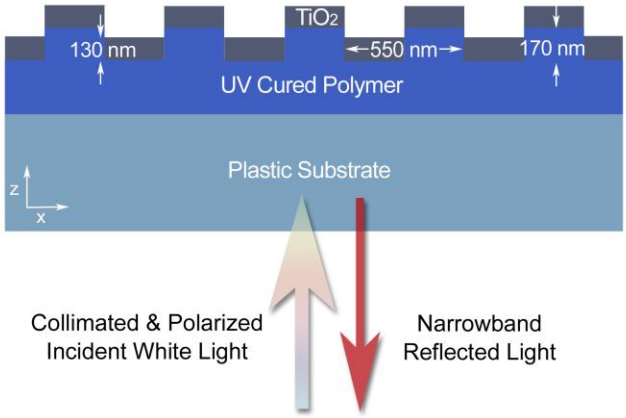

Figure 1.1 Schematic cross section diagram of the photonic crystal biosensor.

1.2.1 PC sensor integrated microfluidic chip

A schematic of the sensor-integrated microfluidic chip is shown at the top of Figure 1.2. The flow channels and the PC biosensor are co-fabricated and self-aligned on a single sheet of flexible plastic. A planar plastic cover is then applied over the flow channels to form the upper surface, and to provide holes for fluid access. The microfluidic network assembly is attached with adhesive to a bottomless 384-well microplate, where it forms the bottom surface. The holes on the fluid chip are arranged so that each microplate well has access to the microfluidic network through one hole. As shown in Figure 1.2, the fluid channels from 5 “analyte” wells are gathered to a single

detection region, where all 5 channels may be monitored at once. A "common" well serves as an access point for introduction of reagents that are identical for all of the flow channels. The common well also serves as a means for applying positive or negative pressure that will drive fluid from the common well into the flow channels, or to pull fluid from the 5 analyte wells at the same rate. The bends in the channel have minimal effect on the overall flow rate of the channels and no flow latency between the channels was observed.

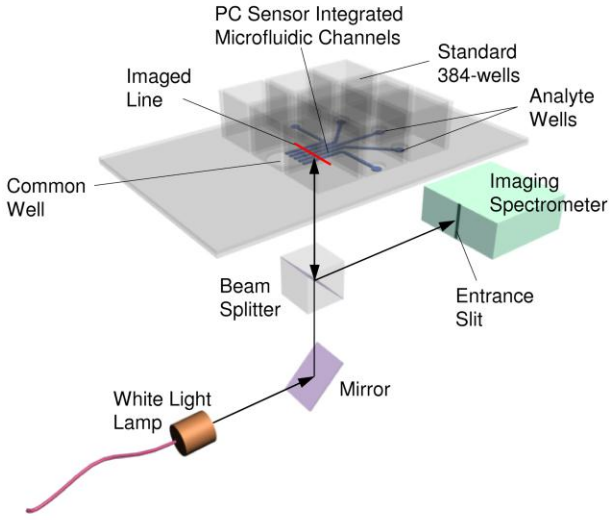

Figure 1.2 Schematic of the PC biosensor integrated microfluidic assay chip with the high resolution imaging detection instrument.

1.2.2 Device fabrication

A room-temperature, low-force replica-molding process utilizing a patterned silicon master and a UV-curable polymer (Gelest, Inc.) is used to fabricate the devices [25]. The fabrication method accurately produces sub-micron features for the PC

structure, while at the same time generating > 10 μm features for the microfluidic channels in a single molding step.

First, a silicon wafer was patterned with a 550 nm period 1-dimensional linear grating structure using deep-UV lithography and reactive ion etching to a depth of 170 nm. The fluid channels were then patterned onto the same silicon wafer using conventional contact lithography and deep reactive ion etching to a depth of 30 μm. As a result of the above processing steps, a negative pattern template of microfluidic channels incorporating a sub-micron linear grating was fabricated. The completed silicon master was subsequently treated with dimethyl dichlorosilane (GE Healthcare) to promote clean release of the replica from the master.

Next, the master wafer pattern was replicated onto a 250 μm thick flexible polyethylene terephthalate (PET) substrate (plastic substrate in Figure 1.1) by distributing a layer of liquid UV curable polymer between the silicon wafer and the PET substrate where the liquid polymer conforms to the shape of the features on the wafer. The liquid polymer was then cured to a solid state by exposure to UV light at room temperature and was subsequently released from the wafer by peeling away the PET, resulting in a polymer replica of the silicon wafer structure adhering to the PET sheet. The sensor structure was completed by depositing 130 nm of titanium dioxide (TiO_2) on the replica surface using electron beam evaporation. For the high index layer of PC sensor structure, any dielectric material that has similar refractive index (n = 2.3) with low optical loss and is inert to biochemical reagents or reactions could also be used. The SEM images of the PC sensor within an open microchannel are shown in Figure 1.3.

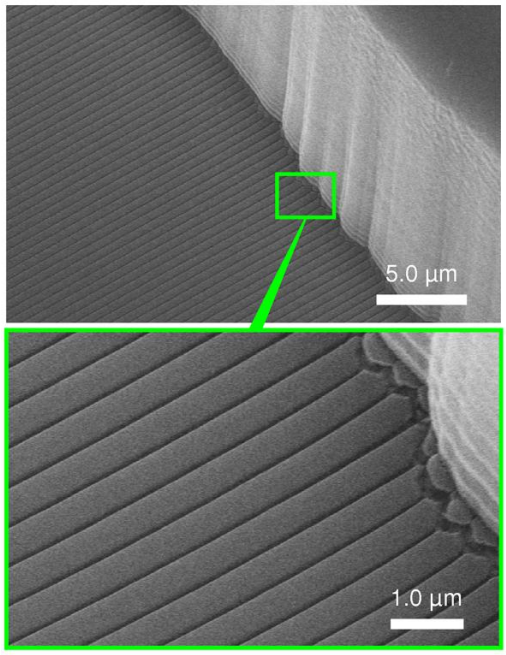

Figure 1.3 SEM images of an open microfluidic channel embedded with the PC biosensor.

The open microfluidic channels were sealed by a separate PET sheet with die-punched 1.6 mm diameter inlet/outlet holes in a pattern corresponding to the locations of the wells of a standard 384-well microplate using a layer of double sided optically clear laminating adhesive film (3M). To complete the packaging, the fabricated polymer microfluidic network assembly was then attached to a bottomless 384-well microplate using an adhesive. The seal provided by the adhesive was very effective and no leakage of fluids occurred.

1.2.3 Detection instrument

A schematic of the biosensor imaging instrument is shown in the bottom of Figure 1.2. White light illuminates the sensor at normal incidence and polarized perpendicular to the sensor grating lines. The reflected light is directed through a beam splitter and an

imaging lens to a narrow slit aperture at the input of the imaging spectrometer. Using this method, reflected light is collected from a line on the sensor surface, where the width of the imaged line is determined by the width of the entrance slit of the spectrometer. The imaging spectrometer contains a 2-dimensional CCD chip (Acton Research) with 2048 × 512 pixels, in which the line image through the slit is divided into 512 pixels and a spectrum with a resolution of 2048 wavelength data points is acquired for each of the 512 pixels imaged. With a spectral measurement range of 830 to 890 nm, the detection instrument sampling interval is 0.0293 nm. Further details on the detection instrument performance specifications can be found in [26]. Upon peak-finding analysis of all 512 spectra, the PWV for each of the 512 pixels is determined, and thus a line of 512 pixels is generated for the PWV image of the sensor.

Based on the PWV imaging mechanism described above, the detection instrument is capable of operating in two different modes: kinetic mode and imaging mode. For kinetic measurements (measuring ΔPWV as a function of time), a motorized stage positions the sensor so that the image line remains fixed upon a single location that intersects 5 flow channels (see Figure 1.2) while the PWV of the PC is measured at fixed time intervals. The measurement interval can be designated by software, where the lower limit (~0.2 sec per measurement) is determined by the integration time of the CCD chip, data analysis/routing time, and processing load on the computer. For the imaging mode (generating 2-dimensional spatial PWV image of the sensor) however, the motorized stage translates the sensor in a direction perpendicular to the image line in small increments, constructing a spatial map of the PC PWV. By this technique a series of lines are assembled into an image through a software program and a large area can be

scanned in a serpentine tiled fashion. The PWV pixel resolution, or the line width of the imaged line for this work, was 22.3 μm. The detection instrument is flexible in terms of its ability to measure reflected spectra from any PC surface, regardless of whether the PC is incorporated into stagnant microplate wells, flow channels, or continuous PC microscope slides.

1.2.4 Device operation

Driving fluids to flow through the microchannels was accomplished by pre-filling one or more microplate wells with solution, and application of pneumatic pressure. After the microplate wells were pre-filled with solution, a silicone cap attached to Teflon microtubing (Cole-Parmer) was inserted into the opening of the well and a pressure regulated lab pneumatic source (2.5 psi) was used to drive liquid through the channels.

1.2.5 Reagents

Phosphate buffered saline (PBS), glutaraldehyde, biotinylated heparin, and human lactoferrin were purchased from Sigma-Aldrich. Starting Block blocking buffer was purchased from Pierce Biotechnology. Streptavidin was purchased from Prozyme. Amine polymer was obtained from SRU Biosystems.

1.3 Experiment

1.3.1 Heparin-lactoferrin assay

Optical biosensors employing surface binding detection are most often used to quantify the affinity of an analyte for its ligand. To provide a realistic demonstration of the assay chip for determining binding affinity between biomolecules, the sensor response to a concentration series of lactoferrin, where the sensor surface is immobilized with heparin, was investigated. Protein interactions with heparin mediate many biologically important process [27]. Therefore, the characterization of the affinity and kinetics of these interactions has been of considerable interest [28]. Lactoferrin is a soluble iron-binding glycoprotein with antimicrobial and anti-inflammatory activity, and heparin is a sulfated polysaccharide that comprises much of the extracellular matrix of many cell types and is used extensively as an anticoagulant drug [27, 29]. For this experiment, the heprin/lactoferrin pair was chosen because it exhibits classical association and dissociation kinetics behavior. Heparin used for the experiment was biotinylated so that it could bind to a layer of streptavidin attached to the sensor surface through a thin polymer coating and bifunctional linker, using an immobilization procedure that has been described previously [30].

Initially, the sensor-integrated microfluidic channels were washed by flowing deionized (DI) water solution from the common well into the channels. Next, the microchannels were filled with a 4% amine polymer solution in DI water and incubated at 25 °C for 24 hr. After washing the channels with DI water, glutaraldehyde (25% in DI water) was flowed through and incubated at 25 °C for 2.5 hr. After washing the channels with DI water, streptavidin (0.5 mg/mL in DI water) was filled and incubated at 4 °C for

24 hr. The channels were then washed with DI water, followed by PBS conditioning. The capture molecule (biotinylated heparin) was then immobilized onto the sensor surfaces of all the channels by flowing the solution (0.1 mg/mL in PBS) from the common well into the channels and incubating at 4 °C for 12 hr, followed by a PBS wash to remove unbound excess biotin-heparin molecules. The 2-dimensional spatial PWV shift image after heparin immobilization/wash obtained by operating the detection instrument in the spatial imaging mode is shown in Figure 1.4. The PWV shift image was acquired on a pixel-by-pixel basis by subtraction of the PWV image before heparin immobilization from the PWV image after wash. PWV shifts are represented by the scale bar from -1.50 to 1.50 nm with red regions representing areas of greatest positive shift. After the heparin immobilization and wash, the unbound regions of the channels were blocked with Starting Block blocking buffer for 1 hr. The channels were then washed with PBS solution and a concentration series of lactoferrin (200, 100, 50, 25 µg/mL in PBS) and a negative control (PBS) was added to each of the analyte wells. After the wells were pre-loaded with the analyte and buffer solutions, the data acquisition from the detection instrument was initiated in the kinetic mode, and the solutions were pumped from each of the analyte wells to the detection area and to the common well. At the end of the association phase, a wash step was performed by rinsing and filling the analyte wells with PBS while the solutions were continuously pumped. After the wash step, the reference channel was filled and pumped with a 2 mg/mL concentration of lactoferrin to determine the maximal binding capability of the heparin-immobilized sensor.

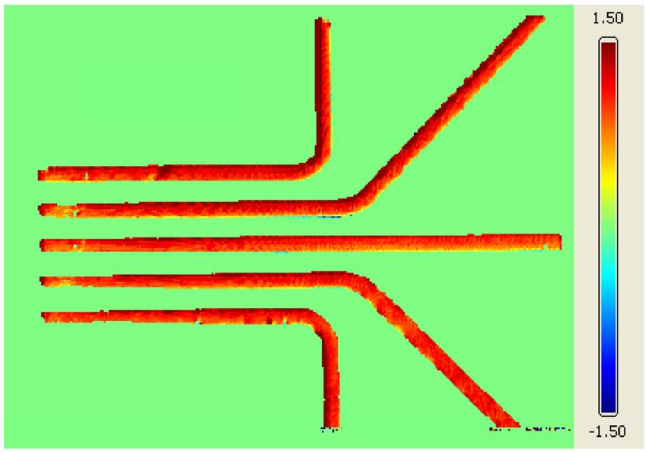

Figure 1.4 Spatial PWV shift image obtained after heparin immobilization and wash. PWV shifts are represented by the color coded scale bar from -1.50 to 1.50 nm with red regions representing areas of greater positive shift.

1.4 Results

The kinetic PWV response of lactoferrin binding to the heparin-immobilized sensor is shown in Figure 1.5. The width of each fluid channel was 300 μm, corresponding to 13 data pixels across (pixel resolution: 22.3 μm), but the PWV response for each channel was calculated by averaging only 7 pixels (156 μm) in the center region across the channels where the fluid flow rate was constant. We assume that the flow rate is constant in the center region of the channel because the channel width is significantly larger than its height. The average standard deviation for the 7 pixel measurement observed was 0.0057 nm. The average PWV shift data in Figure 1.5 were obtained by subtracting the average PWV of the reference channel filled with PBS buffer from the average PWV for each active channel with lactoferrin to remove effects of signal drift that are not due to heparin-lactoferrin interaction. The duration of the association/dissociation measurement was 5 min, with PWV measurements taken at 1 sec

intervals. A negative pressure of -2.5 psi was applied to the common well 65 sec after the initiation of the PWV measurement to introduce the analyte solution over the detection area, and this resulted in a fluid flow rate of 32.7 µL/min for each channel.

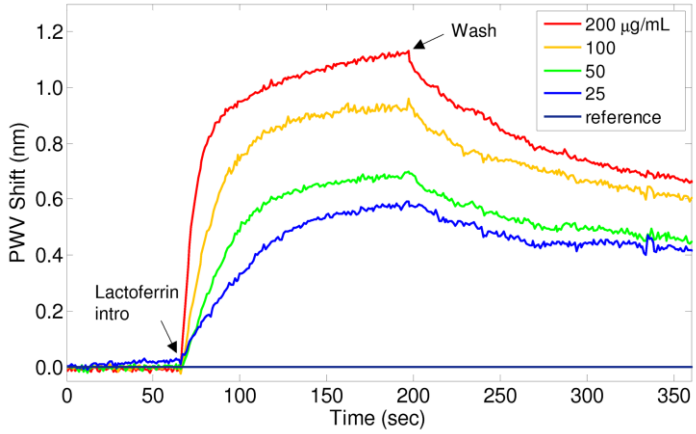

Figure 1.5 Kinetic PWV response of heparin immobilized microfluidic PC sensors for lactoferrin exposure of different concentrations.

Based on the binding interaction between an analyte and a ligand described by the standard equilibrium reaction rate equation, change in the sensor response as a function of time is given by the ordinary dynamic surface binding equation

$$\frac{dR}{dt} = k_a[A](R_{\max} - R) - k_d R \tag{1.1}$$

where [*A*] is the analyte concentration, R_{max} is the maximum capacity of the immobilized ligand, *R* is the biosensor signal which is proportional to the amount of bound molecules [*AL*], k_a is the association rate constant, and k_d is the dissociation rate constant. $R_{max} - R$ is proportional to the amount of ligand available for binding that is not already bound

with analyte molecules. As shown in previous work involving biosensor output response to an analyte introduced within a flow stream, the association phase response is obtained by solving Equation 1.1 at the start of the reaction (*t = 0*) [31].

$$\left.\frac{dR}{dt}\right|_{t=0} = k_a[A]R_{\max} \tag{1.2}$$

Therefore, the plot of initial sensor response rate against analyte concentration results in a linear relationship whose slope is $k_a \cdot R_{max}$ with an intercept of zero. Using this analysis, the association rate constant between heparin and lactoferrin can be determined from the kinetic biosensor response data. Likewise, the dissociation rate constant can be determined by solving Equation 1.1 during the dissociation phase where it is assumed that [A] = 0, resulting in the expression

$$R = (R_0 - R_\infty)\exp(-k_d t) + R_\infty \tag{1.3}$$

where R_0 is the sensor response at the start of the dissociation, and R_∞ is the final steady state response. The dissociation constant, or K_D value for the heparin-lactoferrin interaction, can then be determined from the relationship $K_D = \frac{k_d}{k_a}$.

The initial sensor response rate was determined from the kinetic binding data obtained in Figure 1.5 where the rate was calculated over the linear regions of the binding curves. The initial binding data used to calculate the association rate constant ranges from 4 to 15 data points (sec) from the initial association point. At lower concentration,

the initial slope was calculated using more data points for greater precision since sensor response data at lower analyte concentrations are linear for a longer period of time. The plot of initial sensor response rate as a function of lactoferrin concentration is shown in Figure 1.6. A linear fit was applied to the data using a least squares method with the *y*-intercept set to zero, yielding a slope ($k_a \cdot R_{max}$) of 3.93×10^{-4} nm (µg/mL)$^{-1}$ sec^{-1} with an R^2 value of 0.998. Using the maximum binding capability (R_{max}) determined by introducing 2 mg/mL concentration of lactoferrin, the association rate constant for heparin-lactoferrin binding was calculated as 2.28×10^{-4} (µg/mL)$^{-1}$ sec^{-1}. Based on the dissociation curve fitting, the dissociation rate constant was determined to be $0.0143 \pm 6.49\times10^{-4}$ sec^{-1}. As a result, the K_D value for the heparin-lactoferrin interaction was determined to be 63.1 ± 2.85 µg/mL.

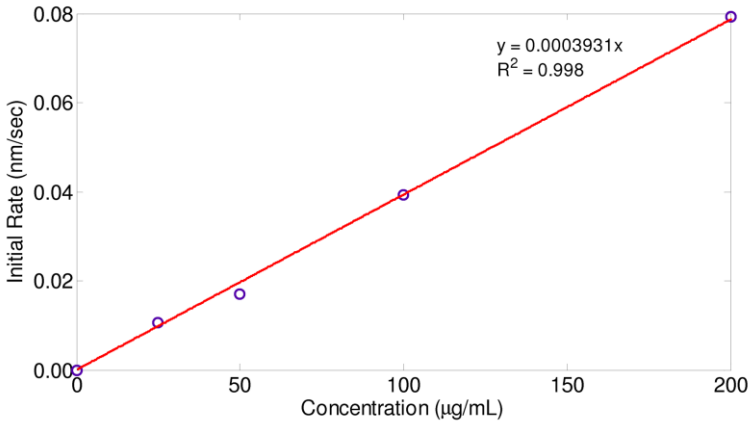

Figure 1.6 Plot of initial binding rate measured between heparin and different concentrations of lactoferrin.

In order to verify the K_D value determined using the PC microfluidic assay chip, another heparin-lactoferrin assay was performed on a commercially available standard

96-well microplate PC biosensor. The biosensor microplate detection of heparin-lactoferrin binding was performed simultaneously with the microfluidic assay using the identical reagents and immobilized ligand surface preparation method. The only significant difference between the biosensor microplate assay and the flow channel assay is that the microplate assay occurs without the use of active flow, resulting in biosensor response rate that is limited by the rate of diffusion of lactoferrin to the bottom surface of the microplate well. Figure 1.7 shows the kinetic PWV response of heparin immobilized PC sensors for lactoferrin exposure of different concentrations in a standard well plate format. In order to perform an end-point concentration series assay without fluid flow, the sensor measurement had to be taken for at least 55 min until a steady state equilibrium response is achieved. Figure 1.8 depicts the end-point PWV shift from the microplate-based sensor, 55 min after the lactoferrin introduction, as a function of lactoferrin concentration ranging from 3.13 to 1000 µg/mL. The data in Figure 1.8 was fit with a dose response sigmoidal curve with an R^2 value of 0.984 and the K_D value was determined to be 60.63 µg/mL.

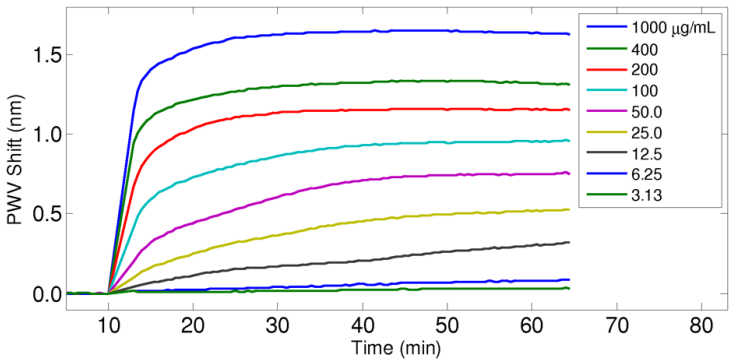

Figure 1.7 Kinetic PWV response of heparin immobilized PC sensors for lactoferrin exposure of different concentrations in a standard well plate format.

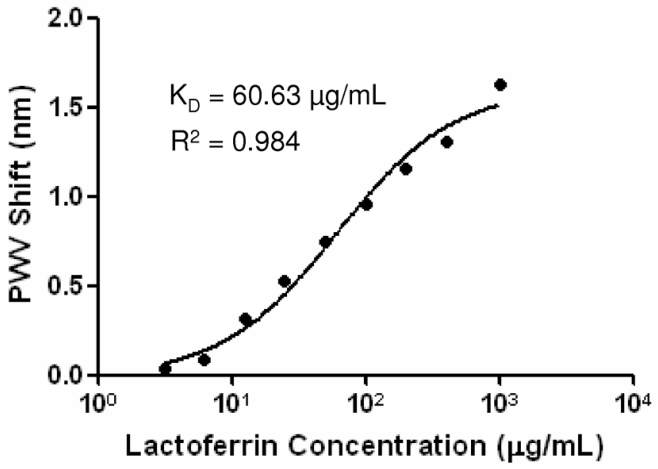

Figure 1.8 Dose response curve for heparin and lactoferrin measured on a conventional well plate based photonic crystal sensor. Data represented as mean ± SD (error too small to be shown), N = 3.

Using the PC integrated microfluidic assay chip, association/dissociation rate constants, and therefore the equilibrium constant (K_D) for heparin-lactoferrin interaction, were determined. To demonstrate the validity of the reaction equilibrium constant determined using the microfluidic based PC sensor chip, an alternate method to determine the K_D value of the reaction was used on a diffusion-limited PC biosensor microplate. As shown in the experiment, the K_D value determined using the microfluidic based PC sensor chip comes within 4.07% of the K_D range determined using the conventional microplate PC sensor.

The K_D value obtained using the PC microfluidic assay chip can also be compared to the heparin-lactoferrin interaction data previously measured using surface plasmon resonance (SPR) biosensors [28]. In that work, the analyte injection flow rate was 30 µL/min and the assay duration was 7 min. Based on the sigmoidal curve fitting of dose response measurement reported in the literature, the K_D value determined by SPR

ranged from 10.50 to 30.94 µg/mL, where K_D variation was attributed to differences in the heparin biotinylation method such as, biotinylation via uronic acids, intrachain bare amines, or the reducing terminus, which in turn affects binding affinity for the analyte. Although a different K_D value than that reported in [28] was obtained from the experiment in this chapter, the value is similar considering the fact that a different surface chemistry method is used.

1.5 Dicussion

The 384-well fluid channel microplate reported here enables low volume kinetic analysis of protein-protein interactions through 5 analyte flow channels with a single control point and offers higher assay density format. This device requires significantly shorter analyte travel distance (5 mm) from the inlet region to the PC detection region, compared to the 96-well microplate based microfluidic sensor format reported previously (64 mm), in which kinetic analysis could not be performed effectively. The shorter analyte travel distance becomes important for accurate kinetic analysis of low analyte concentrations because short analyte travel distance enables very low flow latency and reduces the effect of analyte molecule depletion before reaching the detection region. For the device in this chapter, there was no flow latency between channels whereas with the previous 96-well plate microfluidic device, it was difficult to create low levels of flow latency (flow latency up to 7 sec was observed) [22]. Ideally, the fluid flow rate among all channels should be kept identical for accurate kinetic analysis. Another consequence of long flow path length is the difference in the flow rate observed during the kinetic measurement. The analyte flow rate for the previous literature was 0.442 µL/min, which

is significantly lower than 32.7 μL/min for this work. A flow rate of 0.442 μL/min is too low for accurate kinetic analysis as the reaction rate becomes limited primarily by mass transport, rather than kinetic binding rate. Comparing the active surface area attached with binding sites, the previous 96-well plate based device has 13× more surface area available for binding than the device presented in this chapter. For lower analyte concentration assays, the level of analyte depletion due to the difference in binding site surface area becomes significant. FEM software (COMSOL) was used to verify the difference in the kinetic binding rate between the 96 and the 384-well plate based microfluidic channels. A difference in the kinetic binding rate was observed in the simulation even with the analyte flow rate set to be identical for both cases. With the 96-well plate microfluidic device, reduction in the end-point binding assay time was achieved, but kinetic analysis could not be effectively achieved due to its long channel length. The biosensor microfluidic microplate presented here is capable not only of significantly reducing the assay time, but also of accurately characterizing biochemical kinetic binding constants.

Examination of the methods used to obtain K_D for the same protein-protein interaction using the identical biosensors packaged in two different formats (microfluidic-based detection versus stagnant microplate well detection) yields interesting comparisons in terms of reagent usage and assay time. First, the mass of biotinylated heparin used to generate an immobilized ligand layer in the 96-well microplate format was compared against the mass required to prepare the microfluidic chip. For the standard 96-well biosensor microplate (SRU Biosystems)-based assay for determination of K_D, 5 analyte (lactoferrin) concentrations are required to generate a dose-response curve, and triplicate

wells are used for each concentration. Using 100 μL volumes of 100 μg/mL biotinylated heprarin solution, therefore, results in the use of 150 μg of biotinylated heparin reagent. Performing heparin immobilization within 3 microfluidic channels, using the same concentration solution, required only 15 μg of the ligand. One channel per concentration was used during the experiment in this work, but 3 channels per concentration were used to calculate reagent mass usage for comparison. This appears to be a substantial advantage for the microfluidic approach. However, biosensor microplate wells in the 384-well and 1535-well format are also available (although not used in the experiment reported here). In the 384-well microplate format, for example, only 20 μL of heparin solution would be needed to prepare each biosensor well, resulting in a heparin mass usage of 30 μg, which is similar to the microfluidic mass usage. The mass of lactoferrin analyte required for determining K_D by the two methods may also be compared as well. For the standard 96-well microplate biosensor (SRU Biosystems), 4 different concentrations of lactoferrin were used (25 – 200 μg/mL) with triplicate wells at 100 μL volume for each well for each concentration, resulting in a total lactoferrin mass of 113 μg. In the microfluidic experiment reported here, the same concentrations of lactoferrin were used. With the flow rate of 32.7 μL/min measured per channel, assay association time of 2.2 min, and assuming triplicate flow channels for the experiment, 81 μg of lactoferrin would be used. Therefore, the amount of analyte protein used for the microfluidic-based methods would be slightly less. For the SPR based experiment reported in [28], the amount of lactoferrin analyte consumption would be 74 μg assuming a 30 μL/min flow rate and an assay association time of 2.2 min. A summary of flow rate,

analyte mass required, and measured K_D value for different assay platforms is shown in Table 1.1.

Table 1.1 Comparison of flow rate, analyte mass required, and measured K_D value for different assay platforms.

	96 Well plate	Microfluidics	SPR
Flow rate (μL/min)	0	32.7	30
Analyte mass required (μg)	113	81	74
K_D value (μg/mL)	60.63	63.1 ± 2.85	10.50 to 30.94

With the standard microplate format based biosensors, the reaction kinetics within the plate wells are dominated by the rate of diffusion of analytes to the sensor surface, unless external mixing is provided. Therefore, kinetic biosensor data do not provide reaction rate data on analyte-ligand interactions with the same utility as biosensors incorporated within microfluidic channels, where the analyte diffusion distance is significantly reduced. As a consequence, different analysis methods to determine the K_D value are used for the microplate-based format versus the microfluidic based format. The K_D value analysis for the standard microplate format assay is based on fitting a dose-response curve (end-point analyte concentration series assay) which requires sensor measurements to be taken until equilibrium response is reached. For the microfluidic flow based assay, however, the K_D value determination is based on fitting kinetic association and dissociation data. Therefore, both the association and dissociation rate constants (k_a and k_d) as well as the equilibrium constant (K_D) can be determined with microfluidic based PC sensors, whereas only the K_D value can be determined with the conventional microplate-based format.

Another consequence of mass transport limitation in the standard well plate format is the longer detection time required for the bioassay. In order to perform an end-point concentration series assay without fluid flow, the sensor measurement has to be taken until a steady state equilibrium response is achieved. Therefore the K_D values of the microplate and the microfluidics-based experiments matched, but in the case of microplate based assays, it takes more time for the equilibrium of the sensor response to be reached compared to the microfluidic assay. For the heparin-lactoferrin assay performed on a microplate sensor in this work, the assay time required for the sensor response to reach equilibrium for K_D value determination was 55 min, compared to 5 min for the microfluidic based PC biosensor (Figure 1.5). While the microfluidic chip based assay was run for 5 min, the actual time required for reaction rate constant determination is even less for the initial rate analysis since only a few data points are required after the analyte introduction. Initial rate analysis was used to determine the reaction rate constant because of its simplicity compared to exponentially fitting full association profiles and the need for fewer data points and thus less data collection time. Analyzing the initial portion of the association/dissociation profiles corresponds to binding of only a small fraction of analytes and therefore allows analysis before steric crowding, analyte depletion or mass transport effects become dominant [31]. Therefore, complications arising from non-ideal behavior associated with binding of biomolecules are reduced.

1.6 Conclusion

A PC biosensor integrated microfluidic chip for measuring biomolecular interaction information was developed. The device's capability to determine kinetic binding information was verified through a heparin-lactoferrin concentration series assay using a detection instrument capable of measuring sensor response at high spatial resolution. The microfluidic device reported in this chapter incorporates the traditional advantages of flow-channel based biosensor assays, such as low reagent consumption and rapid response time. The plastic-based replica molding fabrication approach would enable the sensor structure to be inexpensively manufactured and features an external fluid interface that matches a 384-well microplate footprint, and is thus readily compatible with the liquid handling infrastructure that is most commonly available within life science laboratories.

CHAPTER 2: COMPARISON OF LABEL-FREE BIOSENSING IN MICROPLATE, MICROFLUIDIC, AND SPOT-BASED AFFINITY CAPTURE ASSAYS

2.1 Introduction

Label-free biosensors operate through transduction of some intrinsic physical quantity associated with biological analytes that can include small molecules, peptides, proteins, DNA, viral particles, bacteria, or cells [15, 32-36]. Accumulation of analyte upon the biosensor surface results in changes in the mass density, dielectric permittivity, or some other physical quantity that can be transduced to a measurable output signal [19]. The resulting signal is a product of the complex interaction involving the chemical equilibrium between an immobilized capture ligand and the detected analyte, in which both attachment and detachment occur simultaneously. The sensor output signal is also affected by the mass transfer, which may limit the rate of delivery of analyte molecules to the surface, and the loss of available analyte molecules due to scavenging by surfaces other than those incorporating a sensor. Along with the sensor signal output level, the readout background noise, which determines how large a signal must become in order to be considered statistically detectable, is an important quantity. In a biological or chemical sensor system, the sensor's scale factor (that transduces the adsorbed analyte quantity to the output signal), the noise characteristics of the detection method, the surface chemical equilibrium, and the mass transfer of analyte to the surface interact together. This interaction determines the assay detection limits, the amount of time required to accumulate a measureable signal, and whether a detectable signal should be achievable at all for a given system.

Label-free biosensors have often been designed to function in the context of a flow cell – a microfluidic channel that brings the analyte solution to the sensor [21, 37-41]. Typically in these systems, the sensor is "activated" with an immobilized capture ligand by flowing a solution through the channel, resulting in accumulation of capture molecules upstream of the sensor region. By providing sufficient concentration of analyte and flow rate, mass transfer limitations on the detection of analyte can be overcome, but for low analyte concentrations, capture molecules in regions other than the detection region will "steal" available molecules before they can be detected.

Several technologies have demonstrated the capability for increasing the throughput of label-free biosensor measurements by incorporating sensors into the wells of standard format microplates [12, 42]. While increasing the number of assays that can be performed in parallel, these systems have finite assay volumes, a finite number of detectable molecules, and generally no flow. In addition, new technologies have demonstrated the capability for high spectral resolution molecular detection employing ultra high Q-factor resonators [43, 44] and for high resolution imaging detection, in some cases with the ability to also provide kinetic information on binding [12, 45-48] or implementation of arrays of individual sensors on a chip [49-52]. For these technologies, capture ligands are placed in an array of discrete regions of the active biosensor surface or upon discrete sensors in the form of nL – pL volume droplets using technologies capable of performing accurate droplet deposition using physical contact with metal pins, piezoelectric dispensers, and acoustic droplet ejection [53]. In comparison to methods that involve coating the entire inner surfaces of a microplate well or flow channel with capture ligand, spot-based assays can potentially reduce loss of analyte molecules to

unwanted surfaces, thus serving to concentrate detected molecules upon the biosensor active area. Therefore, spot-based methods are expected to provide benefits in achievable detection limits.

Detection of trace quantities of biological analytes by a label-free detection system involves a large number of experimental variables and system design parameters. In the design of an assay, it would be valuable to be able to make accurate analytical or numerical predictions of the magnitude of a measured signal, the evolution of a signal over time, and the conditions under which signals will exceed system noise limits. The goal of the work in this chapter, therefore, is to develop a comprehensive physical model for a general label-free biosensor system that includes the liquid-handling system as an integral part of the model, taking into account the effects of surfaces with which the analyte solution comes into contact. Although the model shown in this chapter is applicable to any label-free biosensor, a single label-free detection platform, the photonic crystal (PC) biosensor, was used as a means for comparing the model to experimentally obtained measurements. The PC biosensor is especially advantageous for this purpose because it has been demonstrated in microplate format [12], microfluidic format [22, 25, 54], and spot-based assays with a high resolution imaging system [55]. Therefore, the PC biosensors with equivalent performance specifications could be implemented in each of these assay formats for direct comparison. As an example assay, the detection of the protein tumor necrosis factor-alpha (TNF-α) using its capture antibody (anti-TNF-α) is simulated and demonstrated. Finite element analysis was performed using COMSOL Multiphysics software, which models phenomena defined in different domains in a fully coupled manner.

2.2 Materials and Methods

2.2.1 Microfluidic sensor fabrication

The fabrication method used for the microfluidic-based sensors is the same as described in section 1.2.2, except that the anti-TNF-α immobilization surface chemistry (described in section 2.2.6) was performed on the open microfluidic channels before sealing with a top PET layer and packaging.

2.2.2 Optical fiber probe instrument

For the standard microplate based bioassay with the entire bottom surface immobilized with capture antibody, a BIND Reader instrument (SRU Biosystems) was used to illuminate the sensor and to detect the reflected signal [12]. To excite the reflected resonance, a broadband near-infrared light-emitting diode illuminates a ~2 mm diameter region of the sensor surface through a 400 μm diameter optical fiber and a collimating lens at normal incidence through the bottom of the microplate. A detection fiber for gathering reflected light is bundled with the illumination fiber for analysis with a spectrometer. A series of 8 illumination/detection heads are arranged in a linear fashion, so that reflection spectra are gathered from 8 wells in a microplate column at once. The microplate sits on a motion stage so that each column can be addressed in sequence. The instrument is capable of measuring 96 wells in 15 sec, though more rapid kinetic information can be gathered from a subset of the plate by measuring a single column at 0.5-sec intervals.

2.2.3 Imaging instrument

For microfluidic-based assays and spot-based microplate assays where PWV shifts of small local features on the sensor surface need to be measured, the optical fiber probe system described above cannot be used since its illumination spot size is 2 mm in diameter. Instead, an instrument that is capable of measuring PWV shifts with high spatial resolution is required. The high resolution imaging detection instrument was described previously in section 1.2.3.

2.2.4 Assay configurations

The four assay configurations are illustrated in Figure 2.1, where the schematics in the figure represent a view of the devices from above looking down into the wells. The areas highlighted in red indicate regions where capture antibodies (ligands) are immobilized. The microfluidic assay with capture antibody immobilized on the entire surface of the microchannel walls, which will be referred to as "Channel-Whole," is shown in Figure 2.1a and the microfluidic assay with capture antibodies locally spotted in a 500 μm wide strip placed on the detection region, which will be referred to as "Channel-Spot," is shown in Figure 2.1b. The arrow in Figure 2.1a indicates the direction of fluid flow during the analyte binding step. In Figure 2.1a and b, six 384 wells are displayed. The standard 384-well microplate assay configuration with the entire bottom surface of the well immobilized with capture antibody, referred to as "Well-Whole," is shown in Figure 2.1c. The assay configuration with 4 spots of capture

antibody (100 µm diameter) placed within a single well of a 384-well microplate sensor is shown in Figure 2.1d, which will be referred to as "Well-Spot." One 384 well is displayed in Figure 2.1c and d.

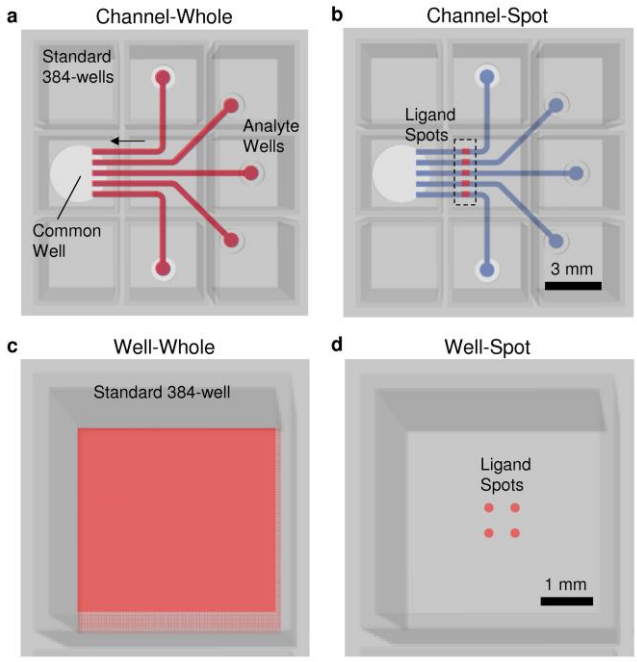

Figure 2.1 Schematic diagram of the assay configurations. The areas highlighted in red indicate regions where capture antibodies are immobilized. (a) Microfluidic sensor with entire bottom surface immobilized with capture antibody (Channel-Whole). The arrow indicates the direction of fluid flow during analyte binding step. (b) Microfluidic sensor with localized ligand immobilization (Channel-Spot). (c) Standard 384-microplate device with entire bottom surface immobilized with ligand (Well-Whole). (d) Standard 384-well micoplate with four immobilized ligand spots (Well-Spot). Six 384 wells are displayed in a, b and one 384 well is displayed in c, d.

2.2.5 Assay reagents

Human TNF-α and biotinylated anti-human TNF-α capture antibody (MAb11) were purchased from BioLegend. Phosphate buffered saline (PBS), Tween 20, and

Glutaraldehyde were purchased from Sigma-Aldrich. BioFX milk blocker solution was purchased from BioFX Laboratories. Streptavidin was purchased from Prozyme. Amine polymer was obtained from SRU Biosystems and 3-glycidoxypropyldimethylethoxysilane was purchased from Gelest.

2.2.6 Surface chemistry

For the microfluidic based assays (Channel-Whole and Channel-Spot), the anti-TNF-α used for the surface chemistry was biotinylated so that it could bind to a layer of streptavidin attached to the sensor surface through a thin amine polymer coating and a bifunctional linker using an immobilization procedure described previously [30]. Initially, the sensor-integrated microfluidic channels were washed by flowing deionized (DI) water solution from the common well into the channels. Next, the microchannels were filled with a 4% amine polymer solution in DI water and incubated at 25 °C for 24 hr. After washing the channels with DI water, glutaraldehyde (25% in DI water) was flowed through and incubated at 25 °C for 2.5 hr. After washing the channels with DI water again, streptavidin (0.5 mg/mL in DI water) was filled and incubated at 4 °C for 24 hr. The channels were then washed with DI water, followed by PBS conditioning. For the Channel-Whole device, the anti-TNF-α solution (0.25 mg/mL in PBS) was placed onto the entire open channel. For the Channel-Spot device, the anti-TNF-α solution was spotted onto the open channels by a piezo array spotter (Perkin Elmer) in a 4 × 30 array with spot-spot distance of 150 µm and each spot utilizing 300±30 pL of volume. The spot array was then repeated twice in the same location to ensure uniform antibody density across the strip with enough spot volume for sufficient immobilization. The

spotting was done inside a closed chamber with humidity control and substrate temperature set to 12 °C. The anti-TNF-α solution on both the Channel-Whole and Channel-Spot devices was then incubated at 4 °C for 18 hr, followed by a PBS wash to remove unbound excess anti-TNF-α. The 2-dimensional spatial PWV image of the Channel-Spot device shown in Figure 2.2 was obtained by operating the detection instrument in the spatial imaging mode. The PWVs are represented by the color scale ranging from 860 to 865 nm, where the red region represents area of greater PWV. It can be observed from the image that the localization of the anti-TNF-α immobilization is achieved. After the anti-TNF-α immobilization and wash, the open microfluidic channels were dried and sealed by a separate PET sheet. Then they were packaged by attaching to a bottomless 384-well microplate using an adhesive as described in the device fabrication section.

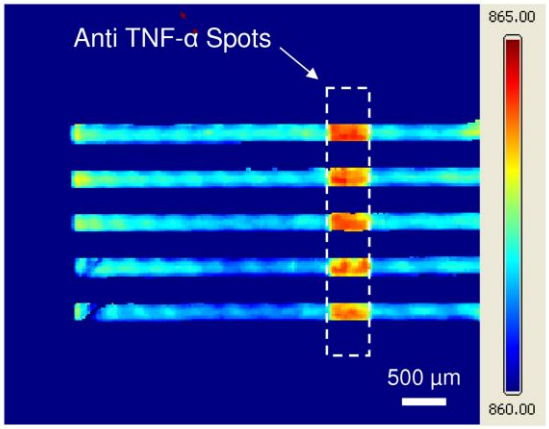

Figure 2.2 Two-dimensional spatial PWV image of the microfluidic PC sensor device after spot-based immobilization of anti-TNF-α. The PWV are represented by the color scale ranging from 860 to 865 nm, where red regions represent areas of greater PWV. It can be observed from the image that the localization of the anti-TNF-α immobilization is achieved.

The anti-TNF-α immobilization on the Well-Whole device was performed using the same reagents and capture antibody surface preparation method as for the Channel-Whole and Channel-Spot devices. The entire sensor surfaces on the bottom of the microplate wells were immobilized with anti-TNF-α by pipetting 50 μL of the solution (0.25 mg/mL in PBS) into each well, incubating for 18 hr at 4 °C, followed by PBS wash and a PWV measurement using the optical fiber probe instrument (SRU Biosystems).

The Well-Spot configuration experiment was performed using a standard PC biosensor microscope slide (1 × 3 inch) and a 384-well size gasket containing a column of 16 wells from SRU Biosystems. The PC biosensor slide was initially surface treated by incubation in an enclosed chamber with 5% 3-glycidoxypropyldimethylethoxysilane in dry toluene at 100 °C overnight. Next, the slide was rinsed with toluene and DI water, and dried with a nitrogen gun. The PC biosensor surface was then spotted with an array of 16 vertical groups of 4 distinct spots of anti-TNF-α in PBS with 0.01% Tween (assay buffer) at 0.5 mg/mL, and allowed to bind for 18 hr at 4 °C. Epoxysilane-based surface chemistry was used for the Well-Spot device because a hydrophobic sensor surface was required to prevent the antibody spots from spreading on the sensor surface, particularly along the PC grating lines. The piezoarray spotting conditions were identical to those used for the Channel-Spot device. After the incubation, the gasket was applied to the sensor surface, where each group of the 4 spots sits in one well. The spots were washed with a large volume of PBS with 2% Tween (wash buffer) and stabilized in 15 μL of PBS with 0.01% Tween, followed by a spatial PWV shift measurement with the imaging instrument operated in the imaging mode.

2.2.7 Binding constant determination

The association and dissociation constants of the TNF-α and anti-TNF-α were determined using the PC integrated microfluidic sensor device through initial rate analysis and dissociation curve fitting, which was previously demonstrated [31, 56]. TNF-α concentrations of 0.2, 1, 5, 10 μg/mL in PBS, and a blank PBS solution as the reference, were introduced into the PC integrated microfluidic chip immobilized with anti-TNF-α on the sensor surface. The wash buffer flow was introduced into the channels 5 min after the introduction of analyte solution in order to observe the dissociation kinetics. Driving fluids to flow through the microchannels during the association/dissociation phase was accomplished by prefilling one or more analyte wells with solution, followed by application of pneumatic pressure. After the analyte wells were prefilled with solution, a silicone cap attached to Teflon microtubing (Cole–Parmer) was inserted into the opening of the common well and a pressure-regulated lab pneumatic source was used to drive liquid through the channels. Due to the short analyte travel distance, no flow latency between the five microchannels was observed when the analyte solutions were driven through. The anti-TNF-α immobilization protocol for the binding constant determination experiment is identical to the protocol for the microfluidic-based TNF-α assay which was described in the previous section. The association constant of the TNF-α and anti-TNF-α pair was determined using the initial rate of the sensor response. The dissociation constant was then determined by fitting the dissociation kinetic curves obtained from each of the four analyte channels (one analyte channel was filled with buffer solution) to the solution of the reaction rate equation during the

dissociation phase. Using this method, the association constant measured for the TNF-α and anti-TNF-α pair was 0.00727 $(\mu g/mL)^{-1}$ sec^{-1} and the average dissociation constant measured was 0.0176 ± 0.00657 sec^{-1}, where ± value represents one standard deviation. The kinetic rate constants measured in this experiment yield a binding affinity of K_d = 0.121 ± 0.0452 μM which is comparable to previously measured values of 0.231 – 0.542 μM for human TNF-α and anti-human TNF-α monoclonal antibodies obtained with a quartz crystal microbalance (QCM) biosensor [57]. The slight difference in the measured binding affinity with the QCM system is likely due to the use of different types of MAb (Z8 and Z12) and different surface chemistry methods (self-assembled thiol on Au) for immobilizing capture antibodies to the quartz crystal.

2.2.8 Assay procedure

For the microfluidic devices (Channel-Whole/Channel-Spot), after the surface chemistry and sealing the open channels, the regions of the channel surface unbound by anti-TNF-α were blocked with 1× concentration BioFX blocking buffer by incubating for 2 hr, followed by a PBS wash. After the surface block/wash, TNF-α concentration series of 40, 200, 1000, 2000 ng/mL (in PBS), and a blank PBS solution as a negative control, were pre-loaded in each of the analyte wells. Next, data acquisition was initiated with the imaging instrument in the kinetic mode, and the solutions were pumped from each of the analyte wells through the detection area and then to the common well by applying 5 inHg of negative pressure at the common well. During the kinetic measurement, the data acquisition line of the imaging instrument was aligned to the center of the localized anti-

TNF-α region of the Channel-Spot device and the same image location was used for the Channel-Whole device.

For the Well-Whole device, regions unbound by anti-TNF-α were also blocked with 1× concentration BioFX blocking buffer by incubating in the wells for 2 hr, followed by a PBS wash. A range of TNF-α sample concentrations (1, 10, 100, 1000, 10000 ng/mL in PBS), and PBS buffer as a reference, were pipetted into separate wells (50 μL). Kinetic measurement of TNF-α binding for the Well-Whole device was performed using the optical fiber probe instrument.

As with the previous assay configurations, sensor regions unbound by capture antibodies of the Well-Spot device were blocked by placing 90 μL of 1× concentration BioFX blocker solution in the wells and incubating for 2 hr. After blocker incubation, the wells were washed with a large volume of the wash buffer and stabilized in 15 μL of assay buffer. After stabilization, the sensor surface was scanned with the imaging detection instrument in the spatial imaging mode to obtain a PWV image after blocker immobilization. The TNF-α samples were prepared in a concentration series of 1, 5, 10, 25, 50, 100, 500, 1000, and 5000 ng/mL in pre-surface blocked centrifuge tubes. The prepared solutions were pipetted directly into each well (50 μL), including two wells with only an assay buffer as reference wells. The anti-TNF-α spots were allowed to incubate with the TNF-α concentration series overnight at 4 °C. The wells were all washed with large volume of wash buffer, stabilized with 15 μL of assay buffer, and a final scan was made with the imaging instrument to obtain PWV image of TNF-α binding.

2.2.9 Computer simulations

Finite element method (FEM) software (COMSOL) was used to model the kinetic sensor response as analyte molecules in the bulk solution are transported and diffused to bind with the capture molecules available on the sensor surface. The governing differential equation used for the analyte concentration in the bulk solution was the convection-diffusion equation listed below as:

$$\frac{\partial c}{\partial t} + \nabla \cdot \left(- D \nabla c + c\vec{u} \right) = 0 \tag{2.1}$$

where c, D, and $\vec{u}$ are the bulk analyte concentration, bulk diffusion constant and fluid flow velocity vector, respectively. For the flow velocity field $\vec{u}$, the parabolic fluid flow velocity profile derived from the incompressible fluid Navier-Stokes equation with no-slip boundary condition was used. At the sensor surface where the ligand-analyte binding reaction occurs, the governing differential equation for the surface bound analyte concentration used was:

$$\frac{\partial c_s}{\partial t} = k_a c \left(\theta_0 - c_s \right) - k_d c_s \tag{2.2}$$

where c_s is the surface concentration of the analyte bound to the sensor surface, k_a is the association rate constant, k_d is the dissociation rate constant, and θ_0 is the surface concentration of active binding site. At the sensor surface, the boundary condition was

represented by coupling of the rate of reaction at the surface with the flux of the reacting species and the concentration of the adsorbed species and bulk species as:

$$\vec{n} \cdot \left(-D\nabla c + c\vec{u} \right) = k_a c\left(\theta_0 - c_s \right) - k_d c_s \tag{2.3}$$

At the inlet of the channel where analyte solution is introduced, the boundary condition used was $c = c_0$ and the boundary conditions for the outlet and the channel wall were $\vec{n} \cdot \left(-D\nabla c + c\vec{u} \right) = \vec{n} \cdot c\vec{u}$ and $\vec{n} \cdot \left(-D\nabla c + c\vec{u} \right) = 0$, respectively. Figure 2.3 shows the mesh used for the FEM simulation of kinetic analyte-ligand binding. A finer mesh was used in the bottom surface region where the highest analyte concentration gradient occurs (analyte molecules in the surface region bind with the surface immobilized ligands). The probe locations for the microfluidics-based sensor were 250 μm (analyte travel distance to the midpoint of the 500 μm wide capture antibody strip across the channels) from the inlet for the Channel-Spot device and 5 mm (analyte travel distance to the imaging instrument's measurement location from the analyte inlet) for the Channel-Whole device. For the simulation parameters, association and dissociation rates of k_a = 0.00727 $(\mu g/mL)^{-1}$ sec^{-1} and k_d = 0.0176 ± 0.00657 sec^{-1} (determined from the binding constant measurement) were used. For the surface density of the capture antibody, 22.5 ng/mm^2 was used based on the analysis of the spatial PWV scan image after the antibody immobilization, where surface mass density to PWV shift ratio of 9 ng/mm^2 per 1 nm PWV shift was used. For the flow velocity within the channel, a parabolic flow profile with maximum velocity of 45 mm/sec was used. This velocity was determined from a 3-dimensional simulation with a negative pressure of 5 inHg applied at the common well.

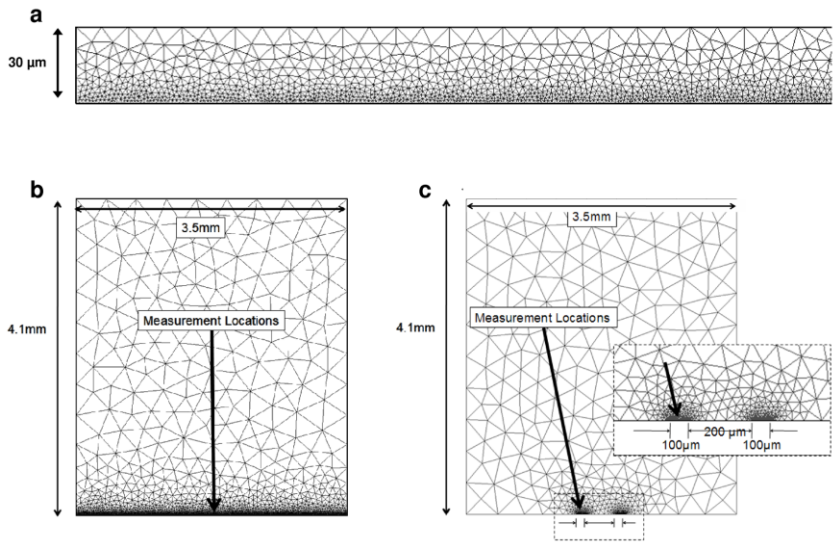

Figure 2.3 FEM mesh used for the assay configurations investigated. (a) Microfluidic based sensor (Channel-Whole/Channel-Spot). (b) Microplate sensor with entire bottom surface immobilized with capture antibody (Well-Whole). (c) Microplate sensor with spotted antibody on the bottom surface (Well-Spot).

2.3 Results

The kinetic binding results from the simulation were compared with the experimental measurements. Figure 2.4 shows the resulting plots comparing the theoretical and experimental kinetic PWV shift of anti-TNF-α immobilized microfluidic assay chips with introduction of TNF-α analyte of concentrations ranging from 0.04 to 2 µg/mL. Figure 2.4a and Figure 2.4b display the kinetic PWV shift for the Channel-Whole and Channel-Spot devices, respectively. The simulation results of the kinetic PWV shift are plotted as thin lines with dash lines indicating upper and lower simulated sensor response levels from ±1 standard deviation associated with the measurement of the kinetic dissociation rate, k_d, and the experimental results are plotted in larger circular

points. The plots show that the experiments terminated earlier than the simulations due to the TNF-α reagent in the analyte wells running out. The analyte wells were not refilled with extra TNF-α reagents because the total analyte quantities consumed from the channel-based experiments would be very large for the duration of the experiment to last over 20 min. This demonstrates the motivation behind using the FEM model to predict the response of label-free biosensor without having to exhaust large quantities of expensive analytes. The differences observed between the theoretical and experimental kinetic shifts could be attributed to the factors that were not included in the FEM model, which are the channel-to-channel variability from the fabrication process, non-uniformities in the capture antibody immobilization density between the channels, and non-specific binding that may still occur in the regions of the channels with no capture molecules despite the blocking step. The factors mentioned above would also cause both the disagreement between theory and experiment for different analyte concentrations and that between the Channel-Spot and Channel-Whole devices. Nonetheless, close general agreement was observed between the computer modeled sensor response and the experimentally measured sensor output for both the magnitude of the wavelength shift and the rate of response without the use of any parameters in the computer model that were not experimentally determined.

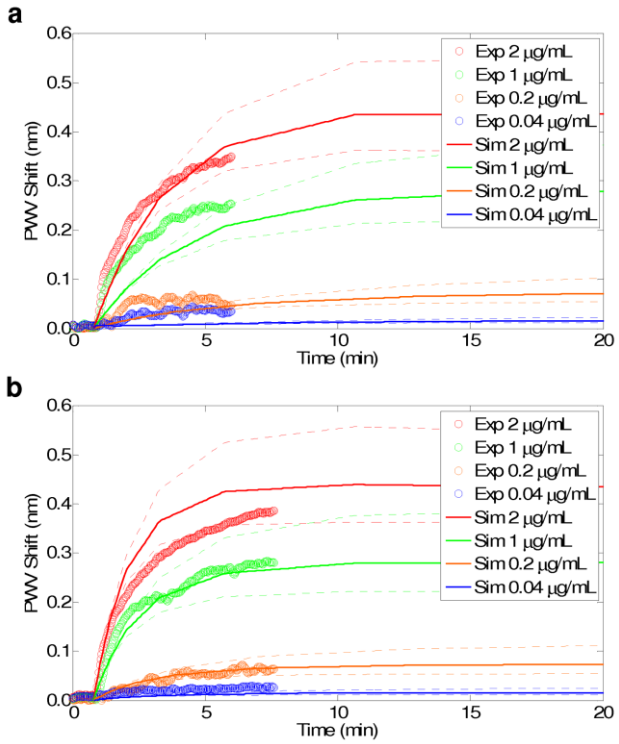

Figure 2.4 Theoretical and experimental comparison of kinetic PWV shift of anti-TNF-α immobilized microfluidic assay chip with introduction of TNF-α analyte of concentrations ranging from 0.04 to 2 µg/mL. (a) Channel-Whole. (b) Channel-Spot.

Figure 2.5 shows the theoretical and experimental comparison of kinetic PWV shift of the Well-Whole device, where TNF-α analyte with concentrations ranging from 0.01 to 10 µg/mL was used. Again, the simulation result of the kinetic PWV shift is plotted as thin lines with dash lines indicating upper and lower simulated sensor response levels from ±1 standard deviation associated with the measurement of the kinetic dissociation rate, k_d, and the experimental result are plotted in larger circular points. As with the results for the microfluidic-based devices, the simulation and experimental results exhibit similar trends, without the use of any artificial scaling parameters in the computer model. For the Well-Whole device, the discrepancies in the kinetic binding

curves can be attributed mainly to the fact that the analyte solution in the well was modeled in the simulation as being completely stagnant. In the actual experiment, fluid motion was introduced during the initial analyte reagent introduction through a pipette leading to rapid analyte convection to the antibody immobilized surface, indicated by consistently higher initial analyte binding rate observed in the experiment. Also in the experiment, some capture antibodies were immobilized on the walls of the well along with the bottom surface, resulting in less than the modeled amount of analyte being available for binding. As with the microfluidic-based sensors, non-specific binding on the regions not immobilized with capture antibodies can affect the binding kinetics.

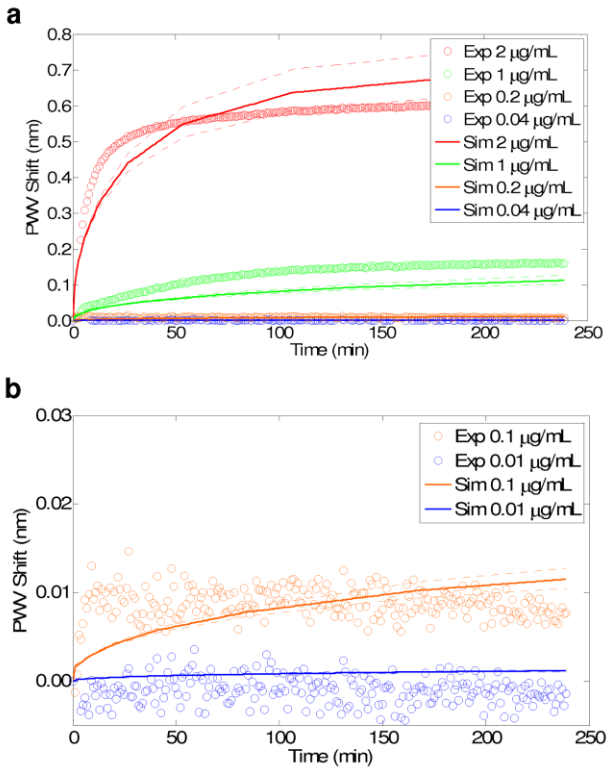

Figure 2.5 (a) Theoretical and experimental comparison of kinetic PWV shift of a Well-Whole device for TNF-α concentrations ranging from 0.01 to 10 µg/mL. (b) Kinetic PWV shift for TNF-α concentrations of 0.01 and 0.1 µg/mL.

For the Well-Spot device, TNF-α binding measurements were made using the high resolution imaging detection instrument operated in the spatial imaging mode. Therefore, the PWV shift data from the analyte binding was obtained as end-points, rather than as kinetic plots, due to the extensive time required to scan through PC slide at high spatial resolution. The end-point PWV shifts of the capture antibody immobilized spots were calculated by considering the PWV shift of pixels in the spot region (active ligand spot) as compared to the PWV shift of regions adjacent to the spots (reference region), before and after injection of TNF-α. Thus, the end-point PWV shift produced by TNF-α binding to the anti-TNF-α spots was obtained by measuring the PWV shift on the active ligand spot before and after the analyte introduction, and subtracting the PWV shift on the reference region before and after the analyte introduction. The analysis method described above can be expressed by the following equation:

$$PWVShift_{endpoint} = \left(PWVShift_{after} - PWVShift_{before}\right)_{active} - \left(PWVShift_{after} - PWVShift_{before}\right)_{reference} \quad (2.4)$$

This calculation was applied to each of the four spots in each well and the average of the four spots was taken to obtain the final PWV end-point value for each TNF-α concentration. The simulated PWV end-point values along with the resulting experimental PWV shift end-point values as a function of the TNF-α analyte concentration are plotted in Figure 2.6. The blue bar represents the computer simulation prediction of the PWV shift endpoint and the red bar represents the endpoint PWV shift

obtained experimentally. The experimental PWV shift values and the simulated PWV shift values show general agreement, exhibiting the same trend. For lower analyte concentrations, larger % coefficient of variation (CV) values associated with lower sensor response levels should be considered for the comparison between the FEM simulation and experiment. The consistently higher PWV shift for the experimental value can be attributed to the slightly higher level of TNF-α antibody activity in the active region from the epoxysilane-based surface chemistry. The standard deviation values associated with the experimental end-point PWV shift plot, represented by the error bars, are mainly from the piezo array ligand spot-to-spot variability existing with the four spots within the well for each TNF-α analyte concentration. The error bars for the simulated end-point PWV shift plot represent upper and lower shift levels from ±1 standard deviation associated with the measurement of the kinetic dissociation rate, k_d.

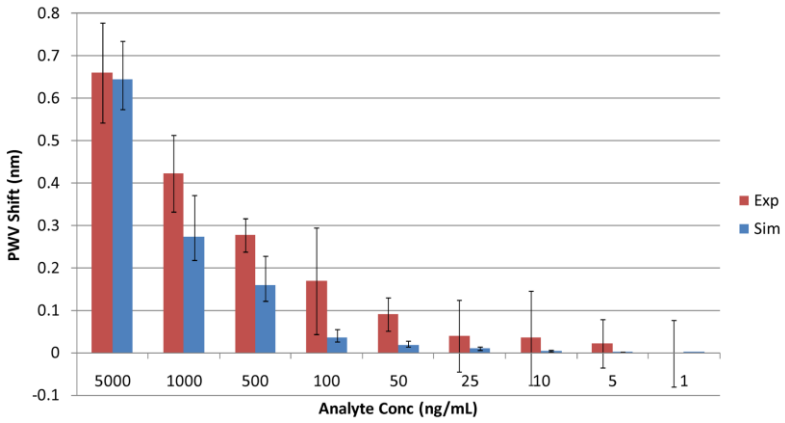

Figure 2.6 Theoretical and experimental comparison of endpoint PWV shift of a Well-Spot format. The blue bar represents theoretical endpoint PWV shift obtained from FEM simulation and the red bar represents endpoint PWV shift obtained experimentally.

2.4 Discussion

With the validation of the simulation results through comparison with experimental measurements, the simulation results can be utilized to obtain predictions of molecular binding interactions in various circumstances. The ability to predict the magnitude of a sensor response signal, the kinetics of the sensor signal (evolution of the signal over time), and the conditions under which signals will exceed system noise limits is extremely valuable. Such capabilities are especially valuable for assays that are difficult to perform experimentally or for assays that must run for long durations. Therefore with the simulation model, the outcome of the bioassay can be predicted at a significantly lower cost without consuming reagents that may be expensive or only available in small quantities. The binding kinetics model was used to examine the equilibrium PWV shift, to compare the amount of time required to reach equilibrium, and to investigate the detection limit for the four different bioassay configurations. The equilibrium PWV shift values obtained from the simulation of the four different assay platforms are shown in Figure 2.7. From the plot, it can be observed that the equilibrium PWV shifts for the Channel-Whole and Channel-Spot devices yielded the highest PWV shifts with identical equilibrium PWV shift amount for both configurations. The Well-Spot sensor yielded a slightly lower PWV shift that is comparable to the microchannel-based sensors, and the Well-Whole device produced the lowest level of PWV shift. Comparing the assay conditions for the four configurations, the analyte sample was continuously replenished for the Channel-Whole/Channel-Spot devices and the amount of analyte volume relative to the ligand spot area was significantly larger for the Well-Spot device compared to the Well-Whole device. Therefore, higher levels of PWV shifts

observed in the Channel-Whole, Channel-Spot, and the Well-Spot device are due to the assay condition in which more analyte molecules are available for binding compared to the case for the Well-Whole device.

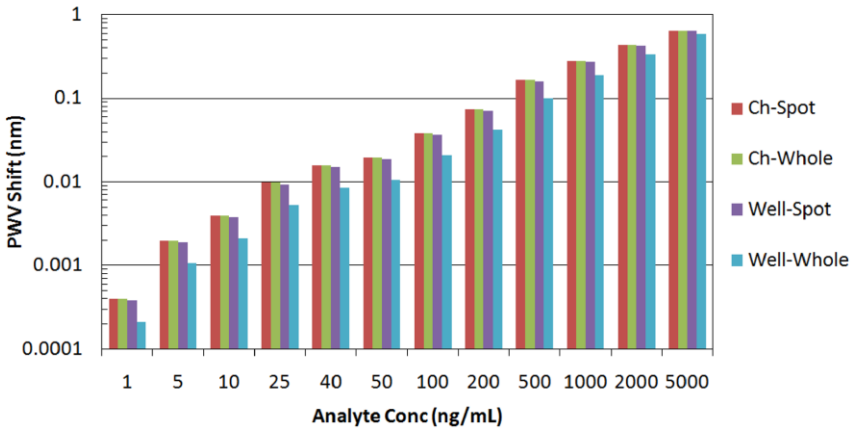

Figure 2.7 Simulation result of final equilibrium PWV shifts of anti-TNF-α immobilized sensors for exposure to TNF-α concentrations ranging from 1 to 5000 ng/mL.

In bioassays, the time to reach equilibrium is important because the assay time directly affects the reagent consumption for flow-channel methods. Consideration of assay time is also important for reagents that lose activity when exposed to room temperature for extended periods of time. The plot for the time required to reach within 5% of the end-point equilibrium value with respect to the analyte concentration for different assay configurations is shown in Figure 2.8. Comparing the time required to reach equilibrium for all devices, the Channel-Whole/Channel-Spot devices reached equilibrium significantly faster than the Well-Whole/Well-Spot devices. This is consistent with the assay condition difference in which the Well-Whole/Well-Spot assays were run without an active flow, resulting in a biosensor response rate that is limited by the rate of diffusion of TNF-α molecules to the bottom surface of the microplate well.

Comparing between the microplate-based devices, the Well-Spot device reached equilibrium faster than the Well-Whole device. Between the microfluidic-based assays, the time required to reach equilibrium for the Channel-Spot device was less than the Channel-Whole device.

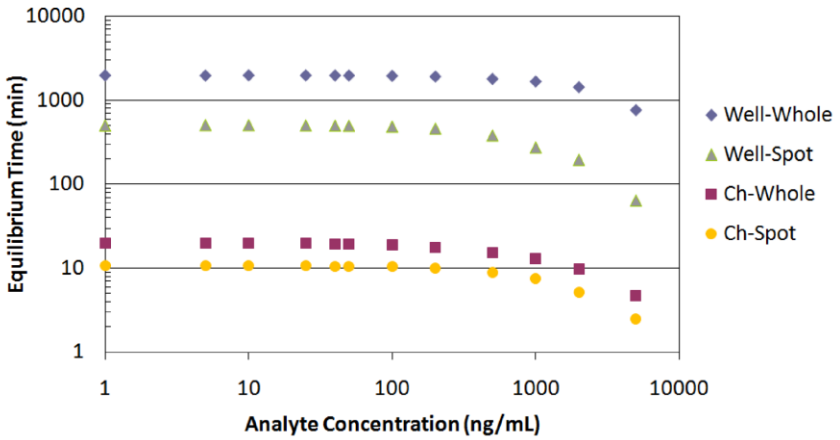

Figure 2.8 Simulation result of time required to reach 5% within the equilibrium PWV shift for all assay configurations.

It should be noted that the equilibrium PWV shift value does not necessarily reflect the biosensor's ability to measure analyte at low concentrations (limit of detection). Both the standard deviation of the PWV signal of the sensor measurement, along with the equilibrium PWV shift information, have to be considered in order to obtain the limit of detection. With the PWV measurement setup used here, the standard deviations of the PWV signal measured were σ = 0.00220 nm for the Channel-Whole/Channel-Spot devices (imaging instrument in kinetic mode), σ = 0.00601 nm for Well-Spot device (imaging instrument in spatial imaging mode), and σ = 0.00203 nm for the Well-Whole device (fiber-optic probe instrument). The difference in the standard deviation of the PWV signal is due to different measurement setups and methods employed for each case

(different probe area and averaging methods). Based on the dose response curve and the sensor readout noise threshold values (3σ), the limits of detection for each of the sensors are 16.7 ng/mL for the Channel-Whole and Channel-Spot formats, 48.4 ng/mL for the Well-Spot format, and 30.9 ng/mL for the Well-Whole format.

For this work, the Channel-Spot device offers the fastest detection time with low probe molecule usage. It also provides the lowest detection limit compared to the Well-Spot/Well-Whole devices and has the added capability of being able to measure kinetic rate constants of biomolecular interactions. Compared to the Channel-Spot format, the Channel-Whole format offers similar advantages and the same detection limit, but longer detection time is required. However, the Channel-Whole format provides the advantage of a simpler assay protocol than the Channel-Spot device since the added equipment for dispensing reagents at specific locations is not required. On the other hand, for the Well-Spot format, the imaging instrument operating in the spatial imaging mode, which had the highest sensor signal standard deviation, was used to measure the PWV shift. Therefore, despite its equilibrium level being comparable to the Channel-Whole/Channel-Spot devices and higher than the Well-Whole device, the limit of detection for the Well-Spot device is higher and time required to reach the detection threshold level is longer. However, an advantage of the Well-Spot format is that probe molecule usage is lowest, making it suitable for assays that involve very expensive antibody reagents that are available only in small quantities. The assay format also has the potential to achieve a lower limit of detection with improvements in the sensor readout noise level. Although the detection times are significantly slower compared to the Channel-Whole/Channel-Spot devices, Well-Whole/Well-Spot devices offer advantages in terms of analyte reagent

consumption since the reagent usage in the microplate devices is significantly lower as continuous flow of reagents is not required. Comparing between the Well-Whole and Well-Spot configurations, the Well-Whole format offers simpler assay protocol and the detection limit is lower with the current measurement setup. For this work, it should be noted that for applications that have high sensor response levels or where the sensor measurement response time is not an issue, microfluidic based devices do not require consumption of large quantities of reagents in comparison to the microplate format. A comparison of the four assay formats investigated in this work is shown in Table 2.1.

Table 2.1 Comparison of PC label-free assay formats.

	Channel - Whole	Channel - Spot	Well - Whole	Well - Spot
Instrument resolution (nm)	0.0066	0.0066	0.0061	0.018
Detection limit (ng/mL)	16.7	16.7	30.9	48.4
Equilibrium response for 50 ng/mL TNF-α (nm)	0.0195	0.0195	0.0105	0.0186
Time required to reach equilibrium for 50 ng/mL TNF-α (min)	19.3	10.60	1965	498
Advantages	Fast detection Largest PWV shift Lowest detection limit Binding constants measureable	Fastest detection Largest PWV shift Lowest detection limit Binding constants measurable	Low analyte consumption Simple assay protocol	Low analyte consumption Lowest ligand consumption
Disadvantages	Large analyte consumption*	Large analyte consumption* Complex assay protocol	Smaller PWV shift Large ligand consumption	Complex assay protocol

* Analyte consumption could be the lowest for applications where sensor reponse level is high and measurement time is not of an issue

2.5 Conclusion

Four different combinations of bioassay formats and capture molecule immobilization methods were investigated through the use of label-free PC biosensors. The assay platforms investigated were the PC biosensor integrated microfluidic device with capture antibody spots immobilized local to the detection area (Channel-Spot), microfluidic sensor device with the entire surface immobilized with capture antibodies

(Channel-Whole), a standard 384-microplate based PC biosensor with capture antibody spots in the well (Well-Spot), and the same 384-microplate sensor with the entire bottom surface immobilized with capture antibodies (Well-Whole). FEM simulation was utilized to model the biomolecular binding kinetics occurring in the different assay platforms, and the results from the model were verified experimentally through the protein-protein binding affinity assay using TNF-α and anti-TNF-α. The simulation model was then used to predict the equilibrium sensor response, sensor measurement time required to reach the equilibrium levels, and the detection limit of the TNF-α protein binding assay, taking into account the conditions for each of the four assay formats. The results were then used to compare the assay performance for each of the assay methods. The microfluidic-based formats (Channel-Spot/Channel-Whole) offered fast detection time, the greatest equilibrium binding of analyte, and lowest detection limit. In addition, the reaction rate constants of biomolecular interaction could be measured. The Well-Spot device offered the lowest ligand consumption with low analyte volume and has the potential for lower detection limit as its equilibrium analyte binding level was similar to that of the microfluidic-based formats. The Well-Whole format offered low analyte consumption with a simple assay protocol. The assay performance results for different platforms obtained from the work in this chapter are applicable to any label-free biosensor system based on surface detection where analyte molecules are brought into contact with the capture molecule immobilized on the sensor surface.

CHAPTER 3: MICROFLUIDIC CHIP FOR COMBINATORIAL MIXING AND SCREENING OF ASSAYS

3.1 Introduction

Microfluidic approaches have been utilized for a wide range of applications including analysis, diagnostics, synthesis, and drug discovery [58-61]. Previous efforts for combinatorial mixing and analysis have focused on continuously flowing microfluidic systems [62-64]. Mixing is performed either by diffusion between contacting streams or by merging droplets in segmented flow, while analysis is performed externally by GC/MS or MALDI-MS. Due to the serial nature of the analyses in these continuously flowing systems, volumes are limited to the nanoliter range, and the complexity of the reaction schemes is limited. To further reduce volume while achieving increased reaction complexity, a finely controlled microfluidic approach that allows for on-chip analysis is required.

In prior work the use of photonic crystal (PC) biosensors was demonstrated as a highly sensitive label-free detection method for performing a wide variety of biochemical and cell-based assays [15, 65]. The sensor surface is designed to reflect only a narrow band of wavelengths with close to 100% efficiency when illuminated with white light at normal incidence. A shift of the reflected peak wavelength value (PWV) to longer wavelengths indicates adsorption (e.g. binding) of a molecular species on the sensor surface. Recently, these label-free PC biosensors were integrated into polymeric continuous flow microfluidic systems [14, 16, 25]. For example, integration of flow channels that originate at individual wells and converge on a row of PC biosensors within a standard 96-well microplate format enabled continuous sampling of each well [22].

This approach was used to determine the binding kinetics of biomolecular interactions. In other work, the ability to detect small molecule binding was also demonstrated with PC biosensors [66]. This PC biosensor-based technology could be greatly enhanced if combined with a mechanism for synthesis and screening of combinatorial arrays of small molecules, a highly desired capability for a wide range of screening applications. A novel platform with these capabilities would require further reduction of reagent volumes and active, parallel fluid handling to create the combinatorial arrays, while retaining on-chip analysis capabilities.

The advent of microfluidic networks with vast arrays of valves by Quake and coworkers [67, 68] has enabled massively parallel chemical syntheses and biological studies in very small volumes (nL – pL), e.g., protein crystallization screening tools [69] and microfluidic gene expression profiling [61]. These chips are typically fabricated via multi-layer soft lithography, the assembly of multiple polydimethylsiloxane (PDMS) membranes that have microscale channels embossed in their surface as negative relief features. Microchannels in the so-called fluid layer are pneumatically filled with liquid using pressurized external feed lines, while microchannels in the so-called control layer are pneumatically actuated at a higher pressure to actively close off fluid lines that they cross at certain locations (Actuate-to-Close or AtC valves). While elegant in routing liquid quanta in microfluidic networks, some aspects of this approach are less desirable with respect to integration of sensing capabilities and the creation of combinatorial arrays. AtC-valve based chips require careful pressure balancing between fluidic and control lines, and with the AtC valves requiring continuous actuation to stay closed, the fluidic layer must be permanently sealed to a substrate to avoid leaking. Furthermore, the chip

continuously must be connected to an external pressure source, which limits portability of the chip, e.g. between a filling station and detection ancillaries.

As an alternative to AtC valves, Mathies has reported the integration of valves that require vacuum actuation of a flat commercially available PDMS layer sealed between two glass slides with channels etched into both layers [70]. These valves can be utilized in multiplexed arrays [71] and have the distinct benefit of being closed at rest. Like the AtC valves above, irreversible sealing is required for operation. Further increasing the number density of these valves, as required for massively parallel combinatorial applications, would be challenging.

In contrast to the above approaches, the implementation of massive arrays of vacuum-actuated Actuate-to-Open (AtO) valves in elastomeric microfluidic networks, which greatly simplifies chip operation and handling, is described in this chapter. To highlight the benefits of this approach, a microfluidic chip capable of metering and mixing a combinatorial array of 200 pL volumes of A × B reactants, resulting in A_1B_1 to A_NB_N combinations that are isolated in individual wells, is created. The bottom surface of each well is equipped with a PC biosensor enabling *in situ* detection of biomolecular interactions in each well.

3.2 Materials and Methods

3.2.1 Actuate-to-open valve arrays

In these chips a control layer and fluid layer are utilized similar to microfluidic networks with AtC valves [68], but fluid lines and compartments are isolated because the AtO valves are passively closed at rest (Figure 3.1). The actuation chamber of an AtO

valve in the control layer is located directly over a small barrier in the fluid layer that separates adjacent compartments or channels. Upon actuation of the control layer compartment with a negative pressure (on the order of 10 psig below ambient), these barriers are lifted to open pathways for fluid routing within the chip. Liquid can be pumped into the chip by applying a negative pressure at an opposing outlet. In addition, liquid can be pulled into a dead-ended channel because actuation of the AtO valves gradually removes trapped air in the fluid channel through the gas-permeable PDMS membrane into the control layer. After the negative pressure is released, the barriers between compartments collapse shut, back into the rest state. The pneumatic lines can then be disconnected from the chip without affecting the sealed, reagent-filled compartments within the chip.

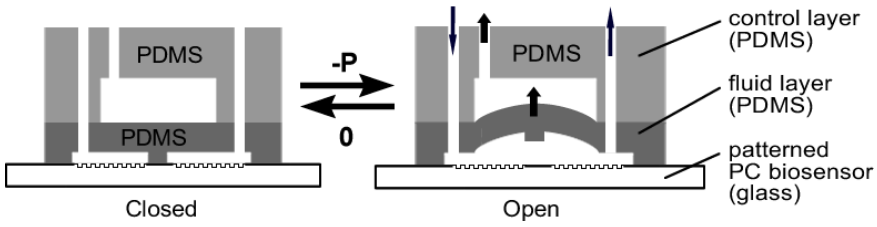

Figure 3.1 Schematic of an Actuate-to-Open (AtO) valve comprised of a pneumatic control layer and a fluid layer, placed on a PC biosensor patterned on a glass substrate. Actuation by applying a negative pressure (right) lifts the barrier between adjacent compartments, allowing for fluid flow. After release of the negative pressure the valve collapses to the closed rest state (left).

As mentioned above, a pressure of about -10 psig is needed to overcome the adhesion between the valve seat and the glass surface, thereby opening the AtO valves. A much lower pressure, down to -1 psig is sufficient to keep AtO valves open. In the rest state (closed), the AtO valves can easily sustain liquid pressures up to 10 psig.

The use of AtO valves as opposed to AtC valves in elastomeric microfluidic networks has many advantages: (i) AtO valves are closed when at rest, the state most valves are in most of the time in just about any application. Compared to the AtC valves, this eliminates the need for continuous actuation at pressures of 5 to 30 psig. (ii) They eliminate the need for irreversible sealing of the fluid layer to a bottom substrate such as a sensor surface (Figure 3.2a). (iii) The gas permeable properties of PDMS eliminate the need for reagent feed lines as fluids are pipetted over inlet ports and are pulled into the fluid lines upon actuation of AtO valves, dramatically reducing dead volume (Figure 3.2b). (iv) In stark contrast to AtC valve-based chips, an AtO chip is highly portable since it can be disconnected from all lines after filling, and moved to a detection platform (e.g. microscope, plate reader). (v) The AtO valve design affords a higher degree of complexity, i.e. a higher density of compartments per unit area because valve area overlaps with compartment area as opposed to being located between compartments.

Constant pneumatic actuation is not required for AtO-based microfluidic systems, making them more amenable for field-portable applications. The absolute pressures needed to actuate AtC or AtO valves are similar and can be achieved in a portable device, for example, using gas tight syringes. However, AtO valves only need to be actuated briefly during filling of a chip (typically less than 30 sec), whereas AtC valves need to be actuated over the course of an experiment (e.g., an incubation over several min to hr) in order to maintain the liquids confined in separate compartments. The gas permeable nature of the PDMS leads to a gradual loss of pressure on AtC valves which a comparably portable system would need to account for.

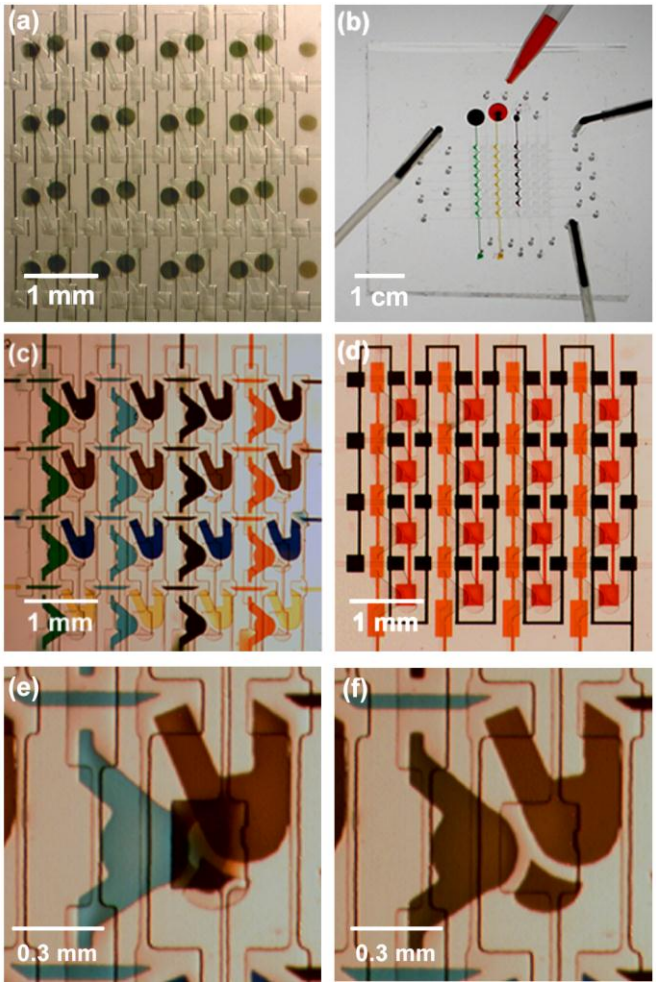

Figure 3.2 (a) Optical micrograph of a 4 × 4 microfluidic chip placed on a patterned array of biosensors. Each well is comprised of two adjacent compartments, each with its own biosensor (dark circles). (b) Photograph of the multilayer microfluidic array chip. Dyed droplets are pipetted at the inlet ports and sucked into the columns by actuation of the appropriate set of valves. (c) Optical micrograph of a 4 × 4 array of wells, highlighting the fluidic layer: the 4 rows and 4 columns are each filled with an aqueous solution of different color to show the combinatorial generation of 16 different combinations of reagents. (d) Optical micrograph of a 4 × 4 array of wells, highlighting the control layer: The 3 sets of valves control filling of the horizontal rows (black squares), filling of the vertical columns (orange rectangles), and the mixing of reagents in adjacent compartments (red squares). (e) Close-up of an individual well in the chip at the very onset of mixing (valve actuated). (f) Mixing is completed following repeated valve actuation over 3 – 5 min.

3.2.2 Design and fabrication of the PC biosensor array chip

A 4 × 4 microfluidic well plate with combinatorial mixing and sensing capabilities was created enabled by the use of AtO valves (Figure 3.2a, b). Each well is comprised of two U-shaped, 200-pL compartments (Figure 3.2c, e). Three separate sets of AtO valves control bi-directional filling and mixing of all 16 wells. The reagents (2 μL each) are pipetted at the inlets of each of the four rows and four columns. Then actuation of the first set of valves (Figure 3.2d, black squares) initiates horizontal flow, filling the rows comprised of the right compartment of each well. Subsequent actuation of the second set of valves (Figure 3.2d, orange recatngles) initiates vertical flow, filling the columns comprised of the left compartment of each well. Upon releasing pneumatic actuation, all valves collapse into their rest state, thereby isolating the reagents in their individual U-shaped compartments. Next, by actuation of the third set of valves (Figure 3.2d, red squares), reagents in all 16 sets of two adjacent U-shaped compartments are mixed. Mixing occurs by diffusion and convection upon 8 – 15 valve actuations and relaxations over the course of 3 – 5 min, as demonstrated with dyes (Figure 3.2e, f).

Next a patterned 4 × 4 array of two circular PC biosensors (D = 250 μm) was fabricated on glass (Figure 3.2a). The porous, dielectric-based PC biosensor gratings were obtained via replica molding as reported previously [14], and photolithography was used to create the patterned array of circles. This pattern exactly maps on the dimensions and relative spacing of the U-shaped compartments of the fluid layer and avoids intra-well leaking, which occurred initially along the grating ridges when using unpatterned, uniform PC biosensor substrates.

3.2.3 Imaging detection instrument

The high resolution imaging detection instrument used for the binding assay was described previously in section 1.2.3, where the instrument was operated in the spatial imaging mode.

3.3 Results

3.3.1 Binding assay

To demonstrate the combinatorial capabilities of the PC biosensor array chip, a proof-of-principle protein/antibody binding assay was performed. The high sensitivity of the PC biosensors requires a method that effectively distinguishes nonspecific binding of antibodies to a sensor surface from an antibody adhering to a specific, surface-immobilized protein. To that end, an experimental and a control compartment were incorporated for each well within the array, with each compartment having its own PC biosensor. Reagents were introduced into the microfluidic network by actuation with a negative pressure, and when the AtO valves were relaxed, all compartments were sealed off, so the chip could be transported for further analysis.

For the binding assay experiment, proteins A and A/G (Pierce Biotechnology) at 0.5 mg/mL in phosphate buffered saline (PBS, Sigma-Aldrich), were incubated for 10 min in the experimental compartments (2nd, 4th row of Figure 3.2c). Sea Block (Pierce Biotechnology) diluted in PBS to 20% by volume was then incubated for 10 min across all compartments as a preventative measure against nonspecific binding. Subsequently,

all compartments were rinsed with PBS; and goat, chicken and human immunoglobulin G (IgG) antibodies (Sigma-Aldrich) at a concentration of 0.5 mg/mL in PBS were incubated for 10 min in the control compartment of each well within the 2nd, 3rd and 4th columns. PBS was introduced in the 1st column as an additional control. After introducing antibodies, the valves were disconnected from the pneumatic lines and relaxed to the closed rest state, sealing off all filled compartments.

At this point, each well contained either PBS or an antibody solution in the left (control) compartment, and PBS in the right (experiment) compartment. The chip was disconnected from all pressure lines and a background scan was taken to record the index of refraction of PC biosensors covered with certain proteins and in the presence (or absence) of certain antibodies in PBS. Next, the chip was reattached to the negative pressure source, and the contents of adjacent control and experiment compartments were mixed by actuation of the mixing valves as explained above (Figure 3.2e, f). A 30-min incubation period with the mixing valve open followed, allowing the antibodies to equilibrate with the surface-immobilized proteins, particularly those in the experiment chamber. The chip was disconnected from the vacuum source and a final scan of the whole array was taken. Subtraction of the background yielded the binding assay results shown in Figure 3.3. Red color indicates strong binding between a given protein and antibody combination. The lack of red coloring in the internal controls, as well as in the microfluidic rows and columns containing only PBS, indicates lack of nonspecific binding as well as a lack of intra-compartmental leaking, which should have been immediately noticed with the protein-antibody assay with the high binding affinities used

here. While the polymeric device is only reversibly sealed to the sensor surface, the AtO valves at rest were sufficient to prevent leaking.

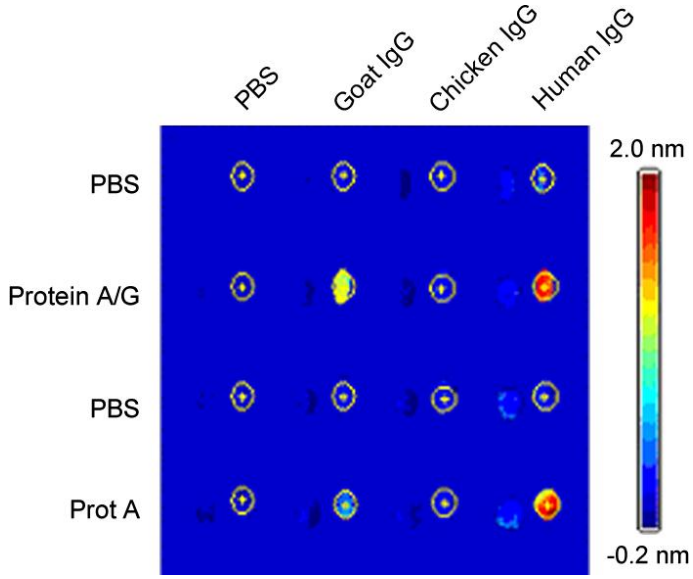

Figure 3.3 On-chip binding assay between proteins (A and A/G) and antibodies (goat, chicken and human). The binding experiment between each protein-antibody combination takes place in the circled compartment on the right of each well, which is compared against a control compartment to its left to rule out nonspecific binding of antibodies. Red coloring within these circles indicates a shift in the PWV, indicative of a binding event.

Finally, the data was analyzed to quantify the extent of binding for each protein-antibody combination. The pixels within each experiment compartment (indicated by the circles in Figure 3.3) were averaged to a single PWV shift value. An average PWV shift for each protein-antibody combination was obtained by subtracting the average PWV of a control compartment from the average PWV of each adjacent experiment compartment to account for signal drift across the array (Figure 3.4). The measured PWV shift values obtained here are consistent with protein/IgG binding experiments previously published [25] where human IgG has a strong binding affinity for both protein A and A/G, goat IgG

has weak binding affinity for protein A but strong affinity for protein A/G, and chicken IgG lacks binding affinity with either protein A nor A/G.

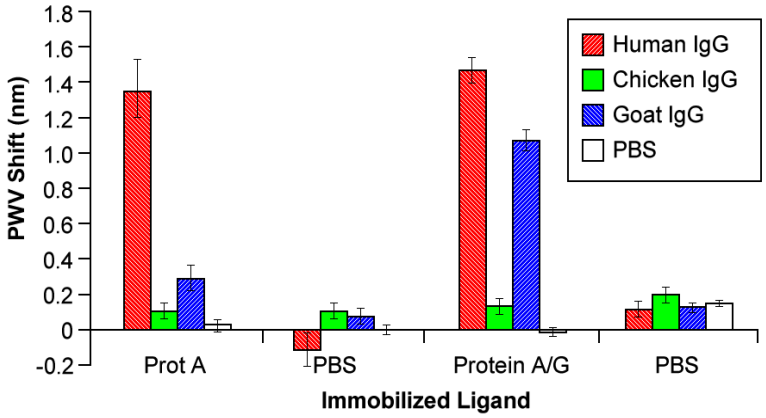

Figure 3.4 Analysis of PWV shifts observed in on-chip binding assay. As expected, human IgG bound strongly to protein A and protein A/G, while goat IgG had a weaker affinity for these proteins. Chicken IgG exhibited a response similar to PBS (±0.2nm), indicative of the lack of binding affinity, as expected.

3.4 Conclusion

The design and fabrication of a microfluidic array chip with combinatorial mixing and on-chip sensing capabilities was demonstrated. A combinatorial matrix of reactions could be performed within 200 pL microfluidic compartments that could be sealed reversibly to a patterned PC biosensor for the determination of binding events. The ability to decouple such AtO-valve based chips from an external pressure source, while retaining the reagents locked up in isolated compartments, greatly simplified their use, particularly for sensing purposes that need to be performed away from fluidic handling capabilities. Current valving technology cannot accomplish this level of post-mixing portability at such high densities. A common problem associated with reversibly sealed

microfluidic chips is their propensity to leak, but the proof-of-principle reaction scheme shown in this chapter using IgG-antibodies demonstrated that AtO-based microfluidic networks do not suffer from leaking issues. Binding events properly correlated to expected results, showing a high fidelity within wells despite the reversible seal. The ability to perform these reactions reliably at such small scales with such ease of use would serve as a great advantage in performing vast array chemistries using much smaller amounts of reagent in combinatorial matrices than presently used in traditional micro-titer plate approaches. Furthermore, the inherent ability of PC biosensors to detect small molecule binding events [66] is preserved in the microfluidic platform presented in this chapter. This microfluidic array chip is thus a promising candidate for chemical synthesis and combinatorial screening applications where multiple steps have to be carried out in parallel in minimal reagent volumes.

CHAPTER 4: SURFACE-ENHANCED RAMAN SCATTERING NANODOME ARRAY

4.1 Introduction

Due to its capability for specific chemical identification through measurement of vibrational energies associated with chemical bonds in molecules, Raman spectroscopy is a powerful and versatile method for label-free molecular identification. As a general purpose analytical method, the applications for Raman spectroscopy span a broad range of fields that includes protein-protein interaction analysis, DNA/RNA hybridization, aptamer conformational change, viral particle detection, bacteria identification, and detection of explosives [72-77]. As first observed by Fleischmann and discovered by Van Duyne, the extremely small Raman scattering cross section may be enhanced when a molecule is in close proximity to a roughened metal surface that supports regions of heightened electromagnetic field intensity [78, 79]. The first demonstrated surface-enhanced Raman spectroscopy (SERS) substrates, providing enhancement factor of ~10^6, were made from electrochemically roughened silver electrodes produced by repeated oxidation-reduction cycles [78-81]. The SERS enhancement factor enables Raman scattering spectra to be gathered rapidly with substantially less laser power, resulting in many detection applications becoming more feasible, provided that the analytes have an opportunity to come into contact with the SERS-active surface.

In recent years, with advancements in nanofabrication technology and the broad availability of computer simulation tools that enable investigation of the interactions of metal/dielectric nanostructures with electromagnetic fields, a wide variety of nanoparticle shapes and structures have been demonstrated as SERS-active surfaces with greater

enhancement factors. For example, colloidal metal (silver or gold) nanoparticle clusters of size ranging from 100 to 150 nm, dispersed in solution, have been used to achieve single-molecule SERS detection, with reported enhancement factors as high as ~ 10^{15} [82, 83]. Nanoparticles with sharp tips, such as metallic "nanocrescents," have demonstrated enhancement factors of > 10^{10} through the effects of electromagnetic field focusing into a small volume when the particle couples with an externally applied laser source through surface plasmons [84]. While SERS approaches using colloidal metal aggregates can produce large enhancement factors, their use is limited due to the lack of enhancement factor reproducibility and low overall "hot-spot" volume density stemming from their sensitivity to random nanocluster morphology [85, 86].

Compared to SERS-active nanoparticles suspended in solution, SERS-active surfaces can be fabricated with engineered three-dimensional topologies using a wide variety of lithography approaches to precisely define desired features. SERS surfaces are especially desirable in applications for which one wishes to measure Raman spectra without adding nanoparticles to a test sample, and for multiplexed arrays of Raman measurements. For example, using electron-beam lithography to fabricate uniform, closely spaced metal nanoparticle arrays of circular, triangular, and square shapes, with interparticle spacing of 75 – 250 nm, reproducible SERS enhancement factors of ~ 10^{6} have been demonstrated [87-90]. Recently, electron-beam lithography patterning of arrays of 200 nm diameter gold nanocylinders has been combined with gold chemical reduction to create "plasmonic nanogalaxy" substrates that exhibit a cascade enhancement effect to generate a spatially averaged SERS enhancement factor up to ~10^{8} [91]. Although large enhancement factors can be achieved using the high resolution

capabilities of electron-beam lithography, the applications of such devices are limited due to the time (and associated cost) of producing such structures over surface areas greater than a few square millimeters. For this reason, there has been intense research interest in the development of processes for creating SERS substrates with a high density of electromagnetic hot spots using procedures that are more amenable to low-cost and large-area fabrication. For example, a soft lithographic molding technique was used to fabricate SERS plasmonic crystals on ~ 20 × 20 mm^2 area and nanowell structure integrated with microfluidic network on a 4 inch wafer, demonstrating enhancement factors of ~ 10^5 and 10^7, respectively [92, 93]. Nanoparticle dimer arrays fabricated by a combination of nanoimprint soft lithography and meniscus force deposition have been demonstrated on a 5 in wafer with enhancement factor up to 10^9 [94]. Likewise, nanosphere lithography (NSL) and metal film over nanosphere (MFON) structures are effective SERS substrates in which arrays of metal triangles (for NSL) or metal domes in a periodic hexagonal lattice (for MFON) are created by deposition of metal thin films over a monolayer of close-packed polymer spheres [95, 96]. MFON has demonatrated SERS enhancement factors of up to 10^7 on substrates with diameter reported as large as 18 mm [97, 98]. Uniform patterning of the MFON surface is dependent upon the ability to produce a defect-free monolayer of ~ 500 – 600 nm diameter polymer or silica spheres using processes such as drop coating, spin casting or controlled withdrawal of the substrate from a liquid bath.

Nanoreplica molding has been demonstrated as a low-cost method for manufacturing periodic surface structures for a variety of applications. The method is performed using low force at room-temperature to produce nanometer scale structures

with high uniformity over a large surface area using a patterned silicon wafer as a reusable molding template. The area of nanoreplica molded surfaces is ultimately limited only by the size of the silicon wafer. However, the process has been adapted for fabrication upon continuous sheets of flexible plastic film in a roll-to-roll process that is capable of producing nanostructured surfaces on the scale of square meters [12]. Nanoreplica molding has been demonstrated for a variety of devices, including photonic crystal label-free biosensor microplates [34, 99], photonic crystal enhanced fluorescence microscope slides [100, 101], distributed-feedback laser biosensors [102], tunable optical filters [103], scaffolds for cartilage engineering [104], microplasma displays [105], and microfluidic channels [22, 25, 56]. In this chapter, a SERS active substrate comprised of a close-packed array of ~ 311 – 377 nm diameter dome structures is demonstrated. The structure is fabricated by a process that combines nanoreplica molding and unpatterned blanket deposition of SiO_2 and Ag thin films. The thin film deposition process is used to control the spacing between adjacent domes with nanometer-scale precision to provide a uniformly distributed array of SERS hot spots that can be produced over a large surface area. An enhancement factor of 10^8 is demonstrated within the hot spot regions, resulting in an enhancement factor of 10^6 when the enhancement is averaged over the entire available surface area.

4.2 Materials and Methods

4.2.1 Nanoreplica molding process

A process flow diagram is shown in Figure 4.1. First, nanoimprint lithography (NIL) (Molecular Imprints) and reactive ion etching were used to pattern an 8 inch (200

mm) silicon wafer with a 2-dimensional array of 300 nm diameter holes (period = 400 nm, depth = 130 nm), in 8 × 8 mm^2 dies to produce a mold template with overall feature dimensions of 120 × 120 mm^2. The completed silicon mold template was subsequently treated with dimethyl dichlorosilane (GE Healthcare) to promote clean release of the replica (Figure 4.1a). Next, a negative volume image of the silicon surface structure was replicated onto a flexible polyethylene terephthalate (PET) substrate by distributing a layer of liquid UV curable polymer (Gelest, Inc.) between the silicon wafer and the PET substrate. The liquid polymer conforms to the shape of the features on the wafer, and is subsequently cured to a solid state by exposure to a high intensity UV lamp (Xenon Inc.) at room temperature (Figure 4.1b). After curing, the molded structure was released from the wafer by peeling away the PET, resulting in a polymer replica of the silicon wafer structure adhered to the PET sheet (Figure 4.1c). The replica molding process results in the formation of a rectangular array of ~ 130 nm-tall polymer cylinders that are separated by ~ 110 nm at their outer perimeters. In order to produce a SERS active surface with metal nanostructures that are separated by distances smaller than 110 nm, SiO_2 was applied over the polymer cylinders by electron-beam evaporation (Figure 4.1d). Through control of the deposited SiO_2 thickness (SiO_2 films of 0, 50, 75, 100, and 125 nm were investigated), the cylindrical polymer surface evolves into a dome structure with a radius that increases with SiO_2 thickness. SiO_2 deposition is followed by application of a 200 nm silver thin film by electron beam evaporation to complete the device (Figure 4.1e).

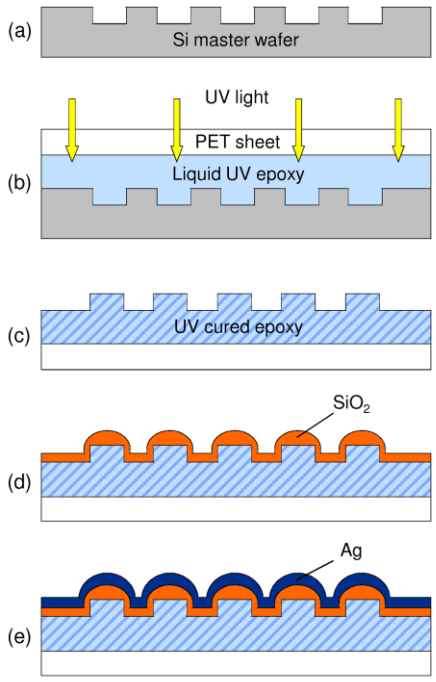

Figure 4.1 Cross section diagram of the nano-scale replica molding process. (a) Fabrication of silicon master wafer template with 400 nm period 2-dimensional circular hole structure using nanoimprint lithography (NIL) and reactive ion etching to a depth of 130 nm. (b) Distribution of liquid-state UV curable polymer between the silicon master wafer and the PET substrate with subsequent solidification by UV light exposure. (c) Release of the PET substrate, resulting in a polymer replica of the silicon wafer structure adhering to the PET sheet. (d) – (e) Deposition SiO_2 followed by Ag on the replicated surface using electron beam evaporation.

The SiO_2 thickness was used to control the nanodome separation distance, which is the most important variable for determination of the SERS enhancement factor. Scanning electron microscope (SEM) images of the fabricated SERS substrates are shown in Figure 4.2. The SEM images were used to measure the separation distance between adjacent domes, resulting in the relationship shown in Figure 4.3. For SiO_2 thicknesses of 0, 50, 75, 100 nm, the separation distance for the nanodome arrays were

84, 59, 33, and 17 nm with the nanodome base diameters of 311, 344, 363, and 377 nm, respectively. When the SiO_2 thickness exceeded 100 nm, the dome spacing reduced to zero, resulting in domes that touch each other, as shown in Figure 4.2e. SEM measurements confirmed that the replica molded structures have a period of 400 nm, as would be predicted by the period of the silicon mold template.

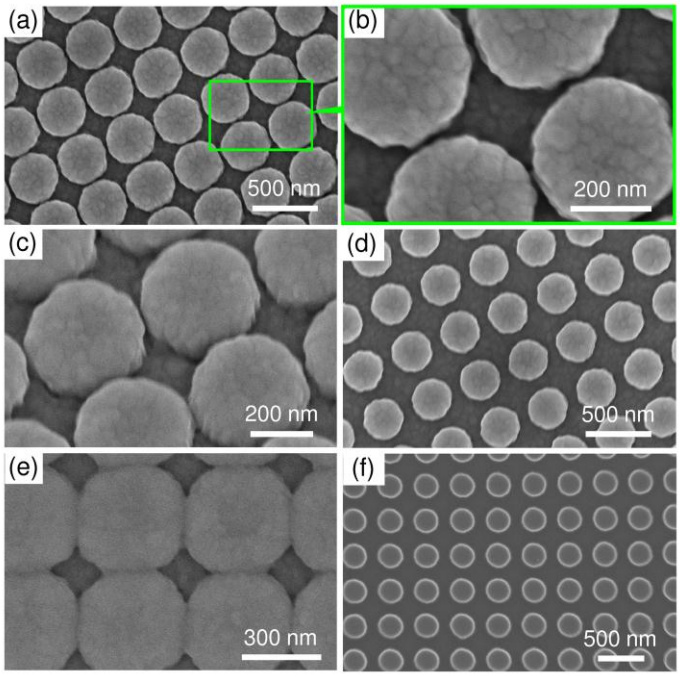

Figure 4.2 SEM images of nanodome array substrates. (a) Ag coated nanodome array substrate with measured separation distance of 17 nm. (b) Close-up view of the nanodome array in (a). (c) Tilted view of nanodome array substrate in (a) and (b). (d) Ag coated nanodome array substrate with measured separation distance of 84 nm. (e) Ag coated nanodome array substrate with domes touching each other. (f) UV cured polymer replica before SiO_2 and Ag deposition.

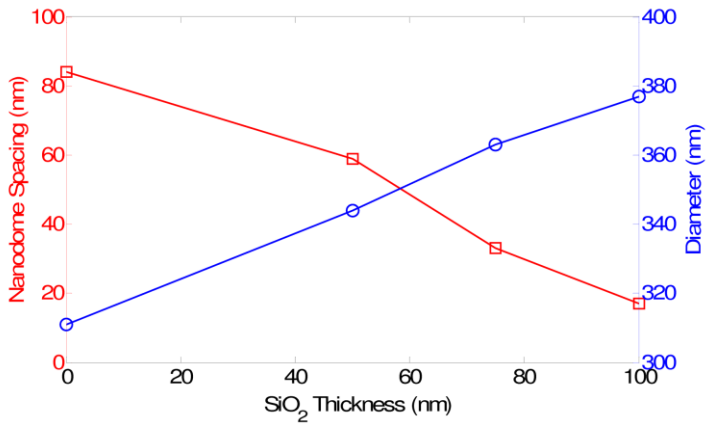

Figure 4.3 Plot of the measured nanodome separation distance (red squares, left axis) and diameter (blue circles, right axis) as a function of SiO2 thickness deposited on the replica.

4.2.2 Computational analysis of field distribution and Raman enhancement

Since the discovery of the SERS phenomenon, two main enhancement mechanisms have been proposed: the chemical enhancement effect and the electromagnetic enhancement effect [81, 106]. Of the two mechanisms, it is believed that the SERS enhancement is dominated by the electromagnetic mechanism, which is due to the enhanced electromagnetic fields originating from the localized surface plasmon resonance (LSPR) effect on both the incident laser and the Raman scattered radiation from the analyte molecules on metal nanostructures. The theoretical SERS enhancement has been described by the following expression [89, 107, 108]:

$$EF_{SERS} \propto \frac{\left|E_{loc}(\lambda_{ex})\right|^2}{\left|E_0(\lambda_{ex})\right|^2} \frac{\left|E_{loc}(\lambda_s)\right|^2}{\left|E_0(\lambda_s)\right|^2} \tag{4.1}$$

where $E_{loc}(\lambda_{ex})$ is the amplitude of the LSPR enhanced local electric field at the laser wavelength, $E_0(\lambda_{ex})$ is the amplitude of the incident electric field (provided by the laser) at the laser excitation wavelength, $E_{loc}(\lambda_s)$ is the amplitude of the enhanced local electric field at the Raman scattered wavelength, and $E_0(\lambda_s)$ is the amplitude of the electric field at the Raman scattered wavelength (radiated by the analyte molecules).

In order to investigate the characteristics of the nanodome array structure as a SERS substrate and to study the effect of inter-dome separation distance on the SERS enhancement (Equation 4.1), finite element method (FEM) modeling using a commercially available software package (COMSOL Multiphysics) was utilized to map the electric field distribution around the nanodomes. The result of the 3-dimensional simulation of the electric field distribution between two adjacent nanodomes within the array is shown in Figure 4.4a with the scale bar on the right side representing the normalized amplitude of the scattered electric field with respect to the incident electric field amplitude. The regions of enhanced electric field are clearly visible in the area between adjacent nanodomes where the separation distance is minimal, as expected due to the coupling effect of LSPR field enhancement. To approximate the conditions in our measurement apparatus, the nanodome arrays in the simulation were excited with a normally incident plane wave at λ = 785 nm, propagating in the –z direction with linear polarization in x direction. The simulation was performed by approximating the metal-coated nanodome structure as having a hemispherical contour. The nanodome array was modeled as a dimer structure with symmetric boundary conditions on the sidewalls of the simulation boundary, in order to reduce the computational load. Figure 4.4b shows the maximum values of Raman enhancement calculated using Equation 4.1 and the FEM

modeled electric field distribution for the laser excitation and the Raman scattered wavelength corresponding to wavenumber shift of ~ 1370 cm^{-1} for nanodome arrays of inter-dome separation distances of 17, 33, 59, and 84 nm, to match the spacings measured by SEM.

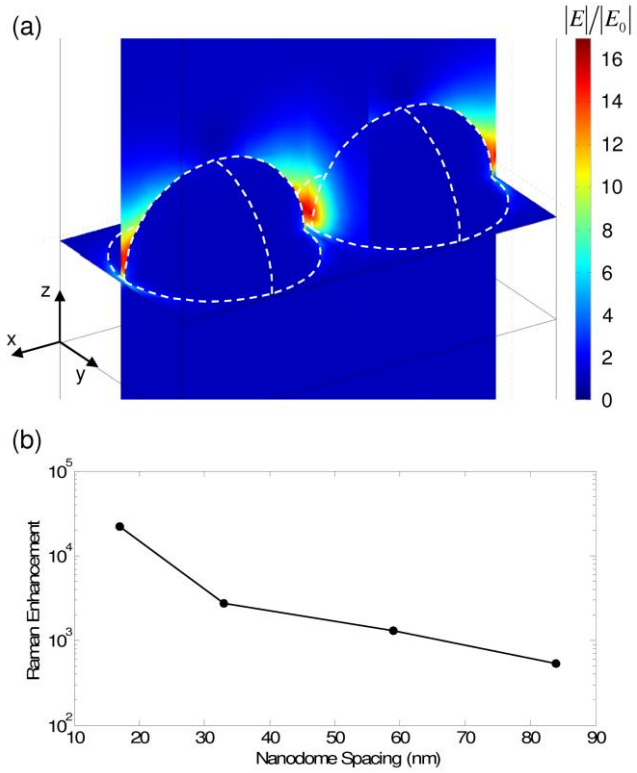

Figure 4.4 (a) 3-dimensional FEM simulation of the electric field distribution around the Ag nanodome particles. Scale bar on the right side represents the normalized amplitude of the scattered electric field with respect to the incident electric field amplitude. The nanodome arrays were excited with an incident plane wave at λ = 785 nm, propagating in the –z direction with linear polarization in x direction. The nanodome array was modeled as a dimer structure with symmetric boundary conditions on the sidewalls of the simulation boundary. (b) Maximum Raman enhancement calculated from the FEM simulation of electric field distribution around the nanodome array for the laser excitation (λ = 785 nm) and the Raman scattered wavelength corresponding to wavenumber shift of ~ 1370 cm^{-1} for inter-dome separation distances of 17, 33, 59, and 84 nm.

4.3 Results

4.3.1 Experimental SERS measurement

In order to experimentally verify the effect of nanodome spacing on SERS intensity, 1 μM rhodamine 6G (R6G) solution was applied to each substrate. The Raman measurement was performed using a 30 mW laser operating at λ = 785 nm, which was focused on the substrate surface by a 10× objective lens (NA = 0.28), resulting in a probe spot radius of 10 μm. SERS photons were collected by the same objective lens, using an integration time of 1 sec. Figure 4.5 shows the experimentally measured relative SERS intensity, defined as $I(d)/I(d_{\max})$ where $d_{\max}$ = 84 nm, of the substrates as a function of nanodome separation distance d plotted as black hollow dots. The SERS intensity values were measured at Raman peak corresponding to a wavenumber shift of 1370 cm^{-1}. The error bars in the figure represent ± 1 standard deviation of the relative intensity obtained throughout five nanodome array substrates for each inter-dome separation distance. Also plotted in Figure 4.5 are the FEM-simulated relative SERS enhancement values with respect to the dome separation distance marked as red squares. As shown in Figure 4.5, SERS intensity/enhancement dependence on inter-dome separation shows a very good agreement between the experimentally measured and simulated values. The inset in the figure shows example SERS spectra for devices with different separation distances ranging from 17 to 84 nm. The SERS intensity observed from the experiment demonstrates that SERS enhancement is very sensitive to inter-dome spacing, and suggests that even higher enhancements may be achievable by controlling the spacing below 17 nm. Interestingly, when adjacent nanodomes are allowed to touch each other (d = 0 nm), the enhancement abruptly drops down to the same value obtained when the

inter-dome spacing is large. This suggests that the majority of the enhancement comes from the "hot spot" region located in the volume region between adjacent nanodomes with enhanced electromagnetic field intensity from inter-dome near-field interaction, consistent with the electric field distribution obtained from the FEM model.

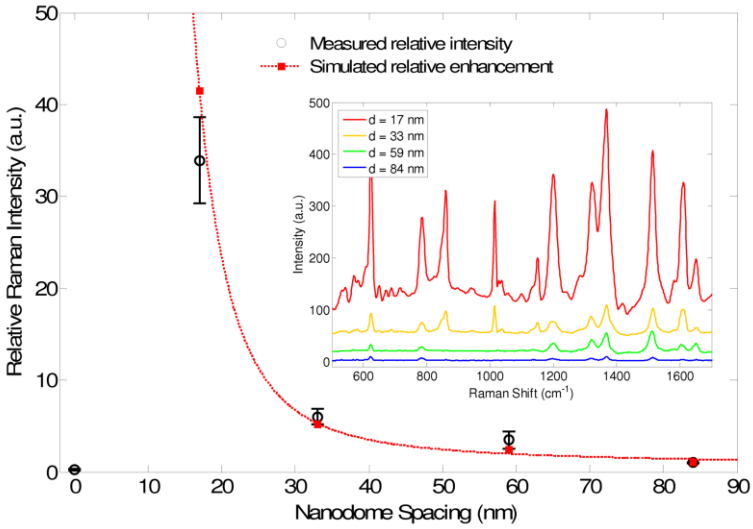

Figure 4.5 Plot of relative SERS intensity I(*d*)/I(d_{max} = 84 nm) as a function of nanodome separation distance, *d*, for 1 μM R6G, measured at the Raman peak corresponding to a 1370 cm^{-1} wavenumber shift. Experimentally measured relative SERS intensities are marked as black hollow dots with error bars representing ± 1 standard deviation for five nanodome array substrates for each dome separation distance (N = 5). Relative SERS enhancement values obtained from the FEM simulation are plotted as red squares. The inset shows example SERS spectra for the nanodome array substrates with different *d* values ranging from 17 to 84 nm.

4.3.2 SERS enhancement factor measurement

In order to experimentally measure the SERS enhancement factor for the nanodome array substrates, a concentration series of R6G molecules (1 nM – 10 μM)

were deposited on SERS sensor surface with an inter-dome separation distance of d = 17 nm. To serve as a reference, 1 mM R6G was also deposited on the same substrate in the area outside of the nanodome region. Using the same detection instrumentation and measurement parameters outlined previously, the SERS spectra shown in Figure 4.6 were obtained.

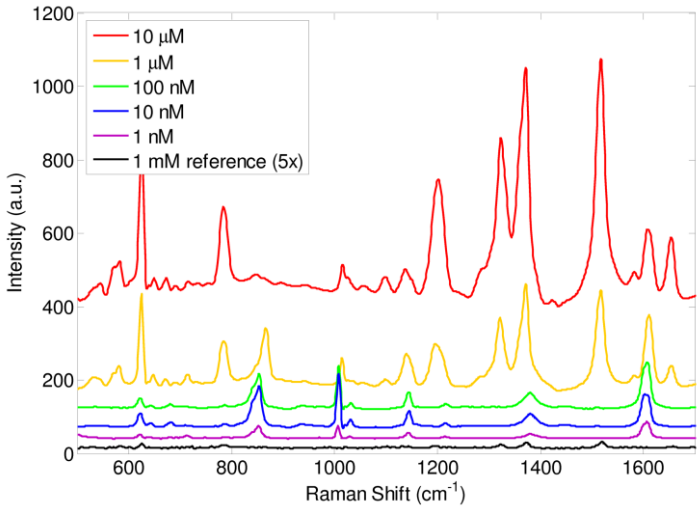

Figure 4.6 SERS spectra of R6G molecules ranging from 1 nM to 10 µM on the nanodome array substrate with *d* = 17 nm and 1 mM R6G on the reference surface without the nanodome array. (The reference spectrum was multiplied by a factor of 5 in the plot.)

The experimentally measured enhancement factor (EF) for a SERS system is given as [108]

$$EF_{SERS} = \frac{I_{SERS} / N_{surf}}{I_{ref} / N_{bulk}} \tag{4.2}$$

where I_{SERS} is the surface enhanced Raman intensity, N_{surf} is the number of molecules within the enhanced field region of the metallic substrate contributing to the measured SERS signal, I_{ref} is the Raman intensity from the reference region, and N_{bulk} is the number of molecules within the excitation volume of the laser spot for the analyte on the reference region. N_{bulk} was calculated by

$$N_{bulk} = \pi r^2 hcN_A \tag{4.3}$$

where r is the radius of the excitation laser spot (10 μm), h is the thickness of the R6G spot on the reference region (0.72 μm), c is the molar concentration of the R6G analyte on the reference region (1 mM), and N_A is the Avogadro's number. N_{surf} was defined to be the number of molecules occupying the volume of the "hot spot" region with high enhancement of the local electric field. The volume of the hot spot region for calculation of N_{surf} was determined from the FEM simulation of the electric field distribution where the enhanced signal was assumed to take place within the region bounded by the volume within which the exponentially decaying enhanced electric field is reduced by a factor of 1/e. Using the SERS intensity from the 1370 cm^{-1} peaks of 1 nM R6G on the SERS active region and 1 mM R6G on the reference region for I_{SERS} and I_{ref}, respectively, the SERS EF was calculated to be 1.37×10^8. The preceding calculation of enhancement factor describes only the enhancement that occurs within the region of highest electric field, and does not account for the fact that only a portion of the available surface area of the substrate is supporting an elevated electric field. To take into account the volume

density of hot spots, the spatially averaged EF can also be calculated. For spatially averaged EF, all analyte molecules within the excitation laser spot volume are assumed to contribute equally to the measured SERS signal. The spatially averaged EF, which represents an underestimation of the local EF from Equation 4.2, provides a more practical, experimentally measured value of the SERS enhancement. The spatially averaged EF of the Ag nanodome array substrate was calculated to be on the order of 3.16×10^6.

4.4 Conclusion

In this chapter, a SERS substrate consisting of a closely spaced array of metal-coated dielectric nanodomes fabricated utilizing a low-cost, large-area nanoreplica molding method was demonstrated. During the fabrication process, the inter-dome spacing was precisely controlled through the thickness of SiO_2 and Ag thin films deposited over a replica molded array of polymer cylinders. FEM simulation was used to investigate the electromagnetic field distribution between adjacent nanodomes, where excellent agreement between the experimentally measured and simulated values for the intensity/enhancement dependence on inter-dome spacing was obtained. Experimentally measured SERS enhancement factor on the order of 1.37×10^8 was demonstrated for the SERS substrate presented in this work. The nanorepolica molding process allows simple, low-cost fabrication of the required surface features over a large area, providing a path towards mass production of SERS substrates with high enhancement factor.

CHAPTER 5: BIOCHEMICAL SENSOR TUBING FOR POINT-OF-CARE MONITORING OF INTRAVENOUS DRUGS AND METABOLITES

5.1 Introduction

In 2008, over 350,000 Americans used dialysis to supplement their kidney function and this number is expected to grow substantially in the future, as > 26 million Americans have chronic kidney disease (CKD) as a result of diabetes and high blood pressure [109, 110]. At the same time, a wide range of drugs and fluids are administered to millions of patients each year using pumped intravenous (IV) delivery, often in combinations used to treat multiple conditions at once. Within the intensive care unit of hospitals, bedridden patients are routinely fitted with urinary catheters that allow drainage of their bladders, and laboratory-based tests are performed upon urine samples to periodically monitor the concentrations of excreted metabolites.

A characteristic that is shared by all three of these common medical practices is the use of disposable sterile plastic tubing to transfer fluids to or from a patient. As the US health care industry seeks to more effectively provide medical treatment, the concept of an "intelligent" system that gathers sensor readings from bodily fluids and provides accurate and timely information on the status of a patient, or that can reduce errors in medication delivery, has gathered momentum [111-113]. However, an important bottleneck to the translation of such systems to clinical practice has been the prohibitive cost/complexity of sensors, and their lack of compatibility with the fluid handling methods commonly used in hospitals.

Detection and identification of the chemical or biological contents of fluid within a flow stream is a critical component of systems used for medical diagnosis and

medication delivery. For example, in-line monitoring of the components of bodily fluids, such as blood and urine, has become a priority in clinical care. In some situations, such as dialysis, a bodily fluid may be analyzed before and after an ex-vivo filtration process in which the fluid will be returned to the patient's body. Likewise, the ability to continuously monitor the contents of an IV line being used to deliver medication to a patient for validation of the desired drug and the presence of contaminants (both chemical and bacterial) would offer a means for minimizing medication errors while at the same time detecting the onset of infections before they become life-threatening. In a similar fashion, the ability to continuously monitor the chemical contents of urine flowing through a catheter would enable noninvasive monitoring of well-established chemical biomarkers for renal function and metabolism.

For detection and identification of analytes in a clinical setting, it is not generally permissible to introduce materials such as chemicals, enzymes, or nanoparticle tags into the liquid media for the sole purpose of facilitating detection. This is true particularly for detection of biochemicals within liquids that are being delivered into a person. For this reason, there is a strong preference to utilize "label-free" detection methods, provided that sufficient sensitivity and selectivity are available. There is also a strong motivation to develop detection methods that can provide continuous information at the point of care, in order to avoid periodic sampling of fluid from tubing connected to patients, which adds a risk of introducing infection and requires tests to be carried out in a separate diagnostic laboratory. Therefore, label-free methods that enable detection of analytes in the flow stream using their intrinsic physical properties, such as dielectric permittivity or molecular vibrational modes, are most desirable. Further, label-free detection that would

allow a sterile sensor to be placed within the flow stream, but that can be monitored from outside the flow stream with a noncontact probing/readout method, is required. Therefore, the goal of work in this chapter is to incorporate label-free, non-contact optical sensors into the internal surfaces of plastic tubing to enable continuous in-line monitoring of the chemical components of the material flowing through the tubing. A schematic of the eventual type of system that could result from the biochemical sensor tubing work is shown in Figure 5.1.

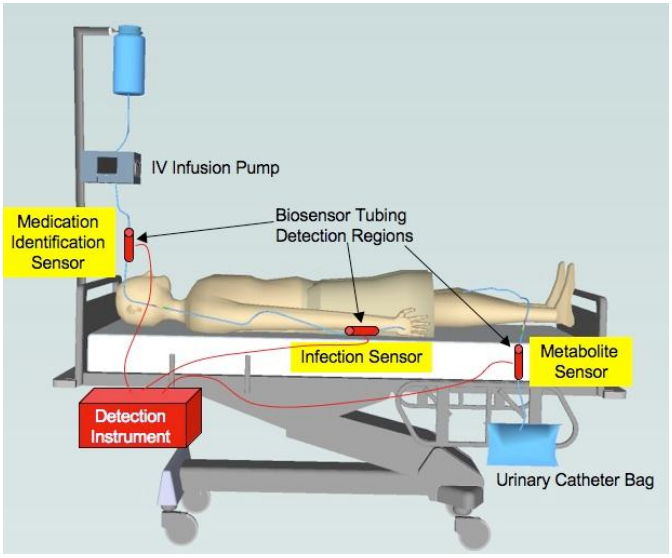

Figure 5.1 Schematic representation of how in-line biosensors would be utilized as part of an intelligent medical system to measure the contents of IV fluid being delivered to a patient or to analyze the contents of a urinary catheter. The sensors are incorporated into disposable plastic tubing and an excitation/readout head clamps around the sensor region. The detection head is connected to the instrument through optical fiber connections.

In this chapter, an IV pain medication (promethazine) and a common urinary metabolite (urea) were used as model analytes to demonstrate the potential for continuous monitoring of an IV delivered drug or kidney function of a patient. A surface-enhanced

Raman scattering (SERS) nanodome structure that is produced upon flexible plastic surfaces by a large-area nanoreplica molding process, described in Chapter 4, was used as the sensor. The nanodome structure provides enhancement of the electromagnetic field from a laser illumination source to provide an easily measurable SERS spectrum that specifically identifies the analyte of interest. Both separate detection and co-detection of promethazine and urea within their clinically relevant concentration ranges, as well as kinetic real-time monitoring of changes in analyte concentration, are demonstrated.

5.1.1 Background

Drug compound – promethazine

Medication errors occurring either in or out of the hospital are estimated to account for 7000 deaths annually, while infusion devices account for up to 35% of errors that result in significant harm (Class 4 and 5) [114]. Current "smart" IV medication safety systems reduce medication delivery errors by providing standard modular-based guidance of the dose and infusion rate through various types of IV administration to the clinicians without the use of sensors [115]. Identification and verification of the chemical contents of a fluid in an IV line being administered to a patient would provide an additional layer of error-checking to ensure that the correct drug and dosage are being delivered.

Promethazine is part of the phenothiazine chemical class that is used medically as an antihistamine, a sedative, and an antiemetic. The maximum recommended concentration for IV administration of promethazine is 25 mg/mL, and overdose can

cause severe tissue injury including gangrene, requiring fasciotomy, skin graft, and/or amputation [116].

Metabolite – urea

Annually, more than 300 million urine analyses are ordered by physicians in the United States [117]. Urine tests are very useful as noninvasive diagnosis and evaluation of kidney function and health of a patient. Urea is the main and final product of protein metabolism; thus its concentration in urine is used as an indicator of the nutritional status of a patient, while its concentration in blood is useful for diagnosis of renal dysfunction. During kidney dialysis, urea is recognized as a marker for a wide spectrum of low and intermediate-molecular mass toxic solutes that accumulate in patients with diminished renal function [118]. Normal physiological levels of urea concentration in blood and urine are 2.5 – 6.7 mM and ~ 333 mM, respectively. In comparison to this normal level, the pathophysiological concentration of urea in blood is 30 – 150 mM, which indicates lost kidney function due to renal clearance failure [117, 119]. In the case of kidney failure, renal replacement therapy in the form of dialysis and transplantation are required in order to sustain the life of a patient.

The most common method for urea detection is an enzyme-colorimetric approach using spectrophotometric detection [120]. However, the colorimetric method involves introduction of additional chemicals/enzymes to fluid samples that could potentially harm patients, and thus is performed by taking a urine sample to a laboratory for analysis. In addition, reagent mixing and incubation steps required for the colorimetric detection make the method unsuitable for real-time monitoring of bodily fluid.

A number of label-free urea sensing methods have been developed including enzyme-based field effect transistors (ENFETs); ion sensitive field effect transistors (ISFETs); and conductometric, potentiometric and optical fiber sensors [119, 121-126]. These sensors involve immobilization of a capture probe molecule, urease enzyme, on the surface of the gate insulator or the sensor. However, uncertainties and variations are associated with label-free sensors immobilized with enzymes. These variations are caused by interference from ammonia and other ionic substances or by change in solution temperature and pH, decreasing the enzyme activity and stability [119]. In addition, immobilization methods through cross-linking cause loss of protein flexibility and hinder the diffusion of analytes, resulting in the sensor performance (sensitivity, response time) being dependent on the method of enzyme immobilization [126]. Therefore, a label-free sensor without the requirement for enzyme or probe molecule immobilization is desirable.

Infrared (IR) absorption spectroscopy has also been used to detect urea in urine by transmitting a selected band of near-IR light through the sample and analyzing the resulting spectral information [127]. The IR absorption spectroscopy method does not involve probe molecule immobilization and is nondestructive and reagentless, thereby permitting in-line identification. However, due to the relatively high detection limit and heterogeneous characteristic of bodily fluid, blood in particular, it is difficult to detect urea with sufficient accuracy.

5.1.2 SERS nanodome tubing

In this chapter, a SERS active surface comprised of an array of closely spaced metal nanodomes was incorporated into a plastic flow chamber connected in series with

flexible tubing as shown in Figure 5.2. Figure 5.2b shows a scanning electron microscope (SEM) image of the nanodome sensor structure incorporated as the bottom surface of the flow cell. Figure 5.2c shows a finite element method (FEM) simulation of the electric field distribution around the nanodomes, in which the greatest electromagnetic fields occur in the gaps between adjacent nanodomes. For SERS surfaces to be viable for an application in which they would be used as a single-use disposable point-of-care sensor, it is necessary to provide a structure that simultaneously provides a large electromagnetic enhancement factor and is made using a low-cost, large-area manufacturable fabrication method. The SERS nanodome sensor used in the present study provides label-free identification/detection of analytes without having to immobilize probe molecules on the sensor surface. The nanodome surface used in the present study is produced on a flexible plastic substrate by a large-area nanoreplica molding process to provide peak enhancement factors of 1.37×10^8. The exemplary experiments on the detection of promethazine and urea demonstrate the clinical potential for SERS sensors incorporated within biomedical tubing. The system could enhance patient safety through prevention of drug delivery errors that occur by administering an incorrect drug or dose, and provide more timely information on the status of a patient through monitoring of urinary metabolite concentration.

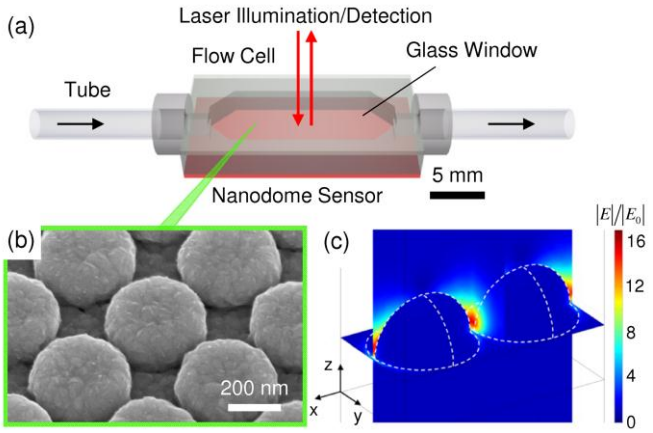

Figure 5.2 (a) Schematic of the biochemical sensor tubing where nanodome sensor structure is incorporated as the bottom surface of the flow cell. (b) SEM image of the nanodome surface. (c) 3D FEM simulation of the electric field distribution (normalized amplitude of the electric field with respect to the incident electric field amplitude) displaying regions of enhanced field between adjacent nanodomes.

5.2 Materials and Methods

5.2.1 Nanodome sensor fabrication – nanoreplica molding process

To produce a template used for the molding, nanoimprint lithography (Molecular Imprints) and reactive ion etching were used to pattern an 8-inch (200 mm) diameter silicon wafer with a 2-dimensional array of 300 nm diameter holes (period = 400 nm, depth = 130 nm), in 8 × 8 mm^2 dies with overall feature dimensions of 120 × 120 mm^2. Next, a negative volume image of the silicon surface structure was formed by distributing liquid UV curable polymer (Gelest) droplets between the silicon wafer and a flexible polyethylene terephthalate (PET) sheet. After curing by exposure to UV light, the molded structure was released from the wafer by peeling away the PET, resulting in a polymer replica of the silicon wafer structure adhering to the PET sheet. Then, 100 nm

of SiO_2 was deposited over the polymer replica by electron beam evaporation, followed by deposition of a 200 nm silver thin film, also by electron beam evaporation, to complete the device. The cylindrical posts created by the replica molding process evolved into rounded dome-like shapes as the deposited films accumulate. The separation distance for the nanodome array was 20 nm with the nanodome base diameter of 380 nm. The details of nanodome fabrication using nanoreplica molding process are described in Chapter 4.

5.2.2 Flow cell incorporated with nanodome sensor

The flow cell was made with a stereolithography system (Viper SLA system, 3D Systems) using an optically clear resin (WaterClear Ultra 10122, DSM Somos). The dimensions of the flow chamber were 18.5 × 7.5 × 3 mm for length, width, and height, respectively. Inlet/outlet cross sectional dimensions of the flow cell were 3 × 1 mm. Two cylindrical openings at the ends of the flow cell were tapped and screwed in with polypropylene barbed adapters (10-32 UNF × 1/8 inch ID, Cole-Parmer) connected to tubing (1/8 inch ID × 3/16 inch OD, TYGON R-3603). The nanodome surface was cut and attached as the bottom surface of the flow cell using UV-cured adhesive (Addison Clear Wave). The top surface window of the flow cell was sealed by attaching a standard No. 2 microscope slide cover glass cut to size using the same UV adhesive.

5.2.3 Detection instrument

The Raman measurement was performed using a 785 nm wavelength diode laser system (Ocean Optics) coupled into an optical fiber. For detection of promethazine, the laser power was set to 100 mW. For detection of urea and urea/promethazine mixture, the laser was set to 150 mW. The laser was focused on the sensor surface by a 10× objective lens (NA = 0.28). SERS photons were collected by the same objective lens, into a QE65000 spectrometer (Ocean Optics) using an integration time of 5 sec for all experiments.

5.2.4 Experiment procedures

Experimental procedures were identical for promethazine and urea as well as for the promethazine/urea mixture. For the concentrations series measurement, promethazine solution was prepared in DI water at 50, 25, 12.5, 6.25, 3.13, and 1.56 mg/mL. Urea solution was prepared in concentrations of 300, 150, 75, 37.5, 18.8, and 9.38 mM also in DI water. Urea and promethazine mixture was prepared in three different combinations: 300 mM, 25 mg/mL; 150 mM, 25 mg/mL; 300 mM, 12.5 mg/mL for urea and promethazine, respectively. Before the SERS measurement, 5 mL of analyte solution was pumped through the sensor tubing manually using a syringe and measurements were taken without flow. After the measurement, the flow cell was washed by emptying the analyte solution and flowing through 10 mL of DI water. Emptying and rinsing with DI water was repeated three times before introducing another analyte with a different concentration. For statistical significance, measurements on the

analyte concentration series were repeated five times (one measurement per analyte concentration in a series).

For the kinetic on/off measurements, the analyte sample and DI water were alternately pumped through the sensor tubing using a separate syringe pump (PHD 22/2000, Harvard Apparatus) for each solution at 60 sec intervals. Tubing from the syringes containing the sample and blank solution were connected to a three-way stopcock valve which was used to alternate the samples flowing into the sensor tubing. The solutions were pumped through the tubing at a flow rate of 5 mL/min. Although typical IV injection rates are significantly lower, a flow rate of 5 mL/min was chosen to facilitate the kinetic experiment and to minimize cross diffusion of analytes at the interface between different solutions as they are being pumped.

For comparison, urea detection was performed using a colorimetric urea assay kit (DIUR-500, BioAssay Systems). The same urea samples used for the experiment on nanodome sensor tubing were diluted 50-fold in DI water prior to the assay. Five µL of urea sample for each concentration, standard urea solution (50 mg/dL) and DI water (blank) were transferred into wells of a clear bottom 96-well plate in triplicates. Then, 200 µL of assay reagent mixture included in the kit was added to each well and incubated for 20 min at room temperature. After incubation, a microplate reader (Synergy HT, BioTek Instruments) was used to measure the optical density of the samples at wavelength of 520 nm.

5.2.5 Data analysis

The background of the raw SERS spectra was removed using a 6th order polynomial fit, followed by signal filtering using Savitsky-Golay parameters with smooth window of 9 and polynomial order of 3. The processed spectra were then subtracted by the reference spectrum from the blank DI water to obtain the final spectra.

5.3 Results and Discussion

5.3.1 Detection of promethazine

Figure 5.3 compares the SERS spectra for promethazine solutions of varying concentrations from 3.13 to 50 mg/mL, the range typically delivered to patients. The SERS spectra of promethazine solution exhibited dominant Raman intensity peaks located at 1030 cm^{-1}, due to the ring-breathing mode of the aromatic rings, and at 1567 cm^{-1} and 1589 cm^{-1}, corresponding to aromatic C=C stretching modes of the molecule [128]. Using the dominant peak located at 1030 cm^{-1} for analysis of promethazine, the inset shows the plot of the average Raman intensity as a function of promethazine concentration with error bars indicating ± 1 standard deviation (N = 5). A linear fit between the Raman intensity at 1030 cm^{-1} and the concentration of promethazine yielded an R^2 value of 0.999. This demonstrates that the nanodome sensor tubing may be used to identify promethazine in solution and the Raman peak magnitude is linearly proportional to its concentration.

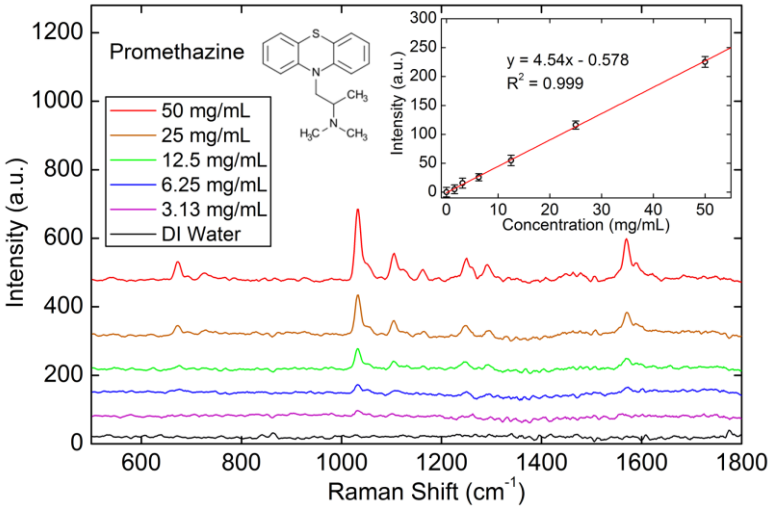

Figure 5.3 SERS spectra for promethazine solution within the sensor tubing. Primary Raman intensity peak for promethazine compound corresponding to the ring-breathing mode of the aromatic rings can be observed at 1030 cm^{-1}. Inset: Raman intensity measured at 1030 cm^{-1} as a function of promethazine concentration with error bars indicating ± 1 standard deviation (N = 5).

In order to investigate the real-time detection capability of the nanodome sensor, SERS measurements were made with 50 mg/mL promethazine solution and DI water alternately pumped through the tubing at 60 sec intervals. Measurements were taken every 5 sec, the same as the integration time of the spectrometer. Figure 5.4 shows the kinetic plot of Raman intensity measured at 1030 cm^{-1} as a function of time. The results indicate that real-time monitoring of solution flowing through tubing can be achieved for the nanodome sensors. Delay in sensor response can be observed due to analyte molecules diffusing across a stagnant flow layer that forms near the surface of the nanodome sensor as solutions are pumped through the flow cell. Considering the typical injection rate used to administer drugs, the delay in sensor response due to diffusion in the stagnant fluid layer should not cause hindrance in detecting medication error before any serious health hazard is posed.

From the kinetic plot, the standard deviation (σ) of the Raman signal measured at 1030 cm^{-1} was 3.51. Based on the linear dose response curve (inset of Figure 5.3) and setting sensor readout resolution as three standard deviations (3σ), the limit of detection for nanodome sensors on promethazine was 2.32 mg/mL. The results suggest that the nanodome sensor tubing system is capable of identifying promethazine compounds and detecting concentrations that are clinically relevant. For example, the system could be used to detect and prevent hazards associated with IV-delivered promethazine over the maximum allowed concentration of 25 mg/mL.

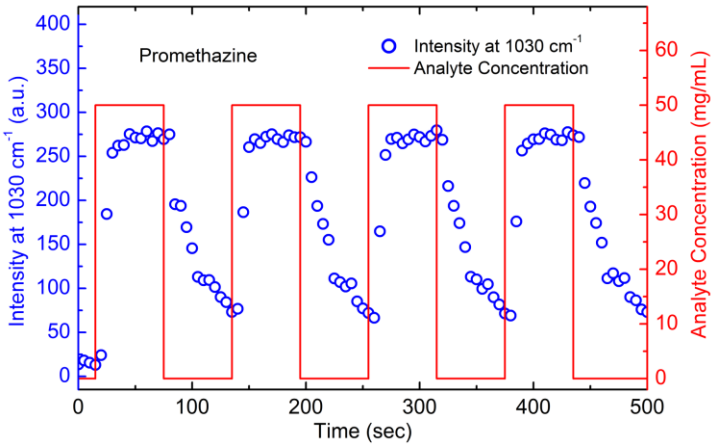

Figure 5.4 Kinetic plot of Raman intensity measured at 1030 cm^{-1} as 50 mg/mL promethazine solution and DI water were alternately pumped through the tubing at 60 sec intervals.

5.3.2 Detection of urea

As with promethazine solution, similar measurements were made for the detection of urea solution flowing through the system. Figure 5.5 compares the SERS spectra for urea solutions of varying concentrations from 18.8 to 300 mM, encompassing the range typically measured clinically. Urea solution exhibited a primary Raman intensity peak at 1000 cm^{-1} from the symmetrical C-N stretch [117]. The inset shows the plot of the

average Raman intensity measured at 1000 cm^{-1} as a function of urea concentration with error bars indicating ± 1 standard deviation (N = 5). A linear fit with an R^2 value of 0.999 was obtained. Again, this demonstrates that the nanodome sensor tubing may be used to identify urea compound in solution and detect its concentration.

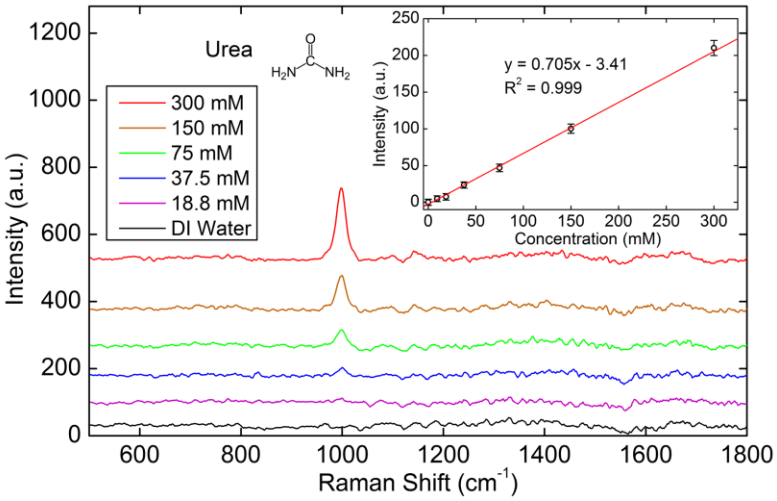

Figure 5.5 SERS spectra for urea solution within the sensor tubing. Primary Raman intensity peak for urea corresponding to the symmetrical C-N stretch can be observed at 1000 cm^{-1}. Inset: Raman intensity measured at 1000 cm^{-1} as a function of urea concentration with error bars indicating ± 1 standard deviation (N = 5).

To investigate the real-time detection capability for urea, SERS measurement was made with 300 mM urea solution and DI water alternately pumped through the tubing at 60 sec intervals. The same integration time and measurement interval as with the promethazine experiment were used. Figure 5.6 shows the kinetic plot of Raman intensity measured at 1000 cm^{-1} as a function of time. Delay in sensor response was observed for the urea measurement as well, but it should not cause issues for real-time detection.

For urea, the standard deviation (σ) for the Raman intensity at 1000 cm^{-1} was 2.54. Based on the linear dose response curve (inset of Figure 5.5) and three standard deviation (3σ) threshold for the sensor readout resolution, the limit of detection for urea was 10.8 mM. The results suggest that the nanodome sensor tubing system is capable of monitoring kidney activity of a patient through identifying and detecting urea well below the typical concentration in urine. The system could also be used to monitor renal clearance failure by detecting urea concentration in blood or dialysate since the detection limit of the system is below the pathophysiological concentration of 30 – 150 mM.

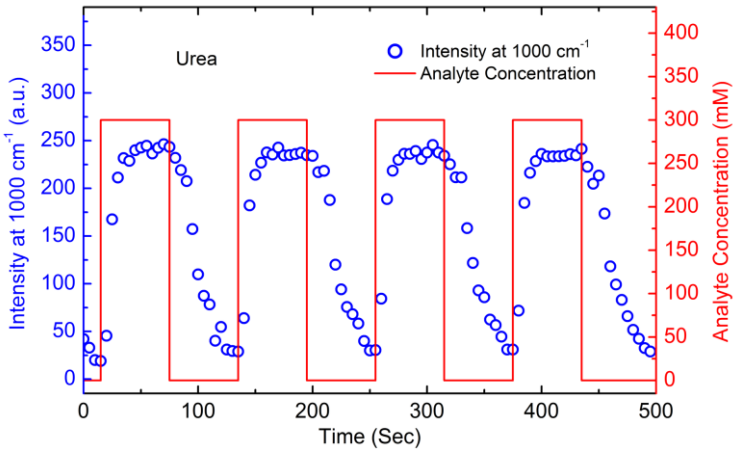

Figure 5.6 Kinetic plot of Raman intensity measured at 1000 cm^{-1} as 300 mM urea solution and DI water were alternately pumped through the tubing at 60 sec intervals.

To verify the accuracy of the nanodome sensor for detection of urea, a standard commercially available colorimetric urea assay kit was also used to measure the concentration of urea samples. Figure 5.7 shows the sensor output comparison between the nanodome sensor and the standard colorimetric assay kit. The comparison data was fitted to a $y = x$ curve with an R^2 value of 0.990.

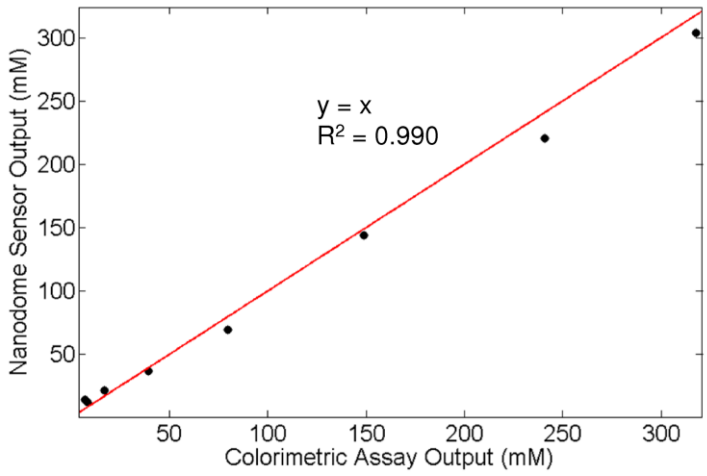

Figure 5.7 Sensor output comparison for urea concentration detection between nanodome sensor and standard colorimetric assay kit.

5.3.3 Detection of urea/promethazine mixture

The ability for multiplexed detection of analytes is useful as multiple drugs or nutrients are often delivered to patients through IV lines in clinical settings. One advantage of SERS-based sensors is their capability for detection of multiple analytes simultaneously when the Raman scattered peaks can be individually distinguished. To demonstrate the multiplexed detection capability of the SERS nanodome sensor, mixture solutions of urea and promethazine at varying concentrations were introduced into the sensor tubing. Figure 5.8 shows the SERS spectra for the urea and promethazine mixtures where primary Raman intensity peaks for both urea and promethazine can be observed at 1000 cm^{-1} and 1030 cm^{-1}, respectively. The intensity values for each analyte were consistent with measurements made with single analyte solution.

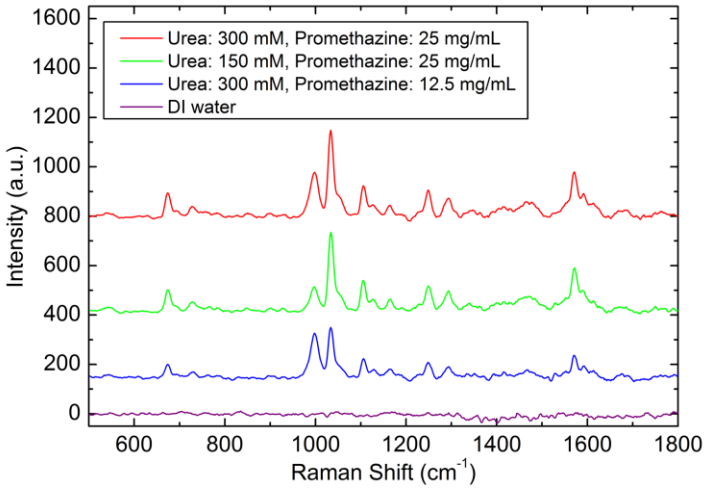

Figure 5.8 SERS spectra for urea and promethazine mixture. Primary Raman intensity peaks for both urea and promethazine can be observed at 1000 cm^{-1} and 1030 cm^{-1}, respectively.

5.4 Conclusion

In this chapter, a SERS nanodome sensor chip incorporated in a flow cell was used for real-time biochemical sensing of fluid within tubing, and proof-of-concept experiments on the label-free detection of urea and promethazine were performed. The potential for an in-line nanodome sensor detection system that would allow real-time detection of fluid samples from patients without taking samples and performing laboratory based tests was demonstrated. The technology may be applied to identify drug compounds that are being administered to patients for enhanced safety for smart infusion systems. The nanoreplica molding method used to make the nanodome substrates is a low-cost, mass-manufacturing process which would allow the devices to be adopted in a clinical setting as disposable single-use sensors. This approach can be further tested by detection of additional metabolites and by detection of urinary metabolites within urine samples, rather than in buffer as demonstrated in this chapter. The potential to develop

the nanodome sensors fabricated upon thin plastic substrates that are highly flexible can also be investigated so that they may be attached to curved surfaces, and incorporated directly into the inner surface of cylindrical tubing. This sensor approach may be applied to the internal surface of many types of liquid containers (test tubes, flasks, graduated cylinders) for a wide range of applications including but not limited to medical detection, food processing, and environmental monitoring.

REFERENCES

[1] N. L. Anderson, A. D. Matheson, and S. Steiner, "Proteomics: applications in basic and applied biology," *Current Opinion in Biotechnology,* vol. 11, pp. 408-412, Aug 2000.

[2] G. MacBeath and S. L. Schreiber, "Printing proteins as microarrays for high-throughput function determination," *Science,* vol. 289, pp. 1760-1763, Sep 8 2000.

[3] A. Pandey and M. Mann, "Proteomics to study genes and genomes," *Nature,* vol. 405, pp. 837-846, Jun 15, 2000.

[4] A. Brecht and G. Gauglitz, "Optical Probes and Transducers," *Biosensors & Bioelectronics,* vol. 10, pp. 923-936, 1995.

[5] A. J. Cunningham, *Introduction to Bioanalytical Sensors*. New York: John Wiley & Sons, 1998.

[6] D. Janasek, J. Franzke, and A. Manz, "Scaling and the design of miniaturized chemical-analysis systems," *Nature,* vol. 442, pp. 374-380, Jul 27, 2006.

[7] N.-T. Nguyen and S. T. Wereley, *Fundamentals and Applications of Microfluidics*. Norwood, MA: Artech House, Inc., 2002.

[8] P. Yager, T. Edwards, E. Fu, K. Helton, K. Nelson, M. R. Tam, and B. H. Weigl, "Microfluidic diagnostic technologies for global public health," *Nature,* vol. 442, pp. 412-418, Jul 27, 2006.

[9] B. Cunningham, P. Li, B. Lin, and J. Pepper, "Colorimetric resonant reflection as a direct biochemical assay technique," *Sensors and Actuators B-Chemical,* vol. 81, pp. 316-328, Jan 5, 2002.

[10] B. Cunningham, B. Lin, J. Qiu, P. Li, J. Pepper, and B. Hugh, "A plastic colorimetric resonant optical biosensor for multiparallel detection of label-free biochemical interactions," *Sensors and Actuators B-Chemical,* vol. 85, pp. 219-226, Jul 25, 2002.

[11] B. T. Cunningham and L. Laing, "Microplate-based, label-free detection of biomolecular interactions: applications in proteomics," *Expert Review of Proteomics,* vol. 3, pp. 271-281, Jun 2006.

[12] B. T. Cunningham, P. Li, S. Schulz, B. Lin, C. Baird, J. Gerstenmaier, C. Genick, F. Wang, E. Fine, and L. Laing, "Label-free assays on the BIND system," *Journal of Biomolecular Screening,* vol. 9, pp. 481-490, Sep 2004.

[13] L. L. Chan, M. Pineda, J. T. Heeres, P. J. Hergenrother, and B. T. Cunningham, "A general method for discovering inhibitors of protein-DNA interactions using photonic crystal biosensors," *ACS Chemical Biology,* vol. 3, pp. 437-448, Jul 2008.

[14] B. Lin, P. Li, and B. T. Cunningham, "A label-free biosensor-based cell attachment assay for characterization of cell surface molecules," *Sensors and Actuators B-Chemical,* vol. 114, pp. 559-564, Apr 26, 2006.

[15] B. Lin, J. Qiu, J. Gerstenmeier, P. Li, H. M. Pien, J. Pepper, and B. Cunningham, "A label-free optical technique for detecting small molecule interactions," *Biosensors & Bioelectronics,* vol. 17, pp. 827-834, Sep 2002.

[16] L. L. Chan, S. L. Gosangari, K. L. Watkin, and B. T. Cunningham, "A label-free photonic crystal biosensor imaging method for detection of cancer cell cytotoxicity and proliferation," *Apoptosis,* vol. 12, pp. 1061-1068, Jun 2007.

[17] U. Jonsson, L. Fagerstam, B. Ivarsson, B. Johnsson, R. Karlsson, K. Lundh, S. Lofas, B. Persson, H. Roos, I. Ronnberg, S. Sjolander, E. Stenberg, R. Stahlberg, C. Urbaniczky, H. Ostlin, and M. Malmqvist, "Real-Time Biospecific Interaction Analysis Using Surface-Plasmon Resonance and a Sensor Chip Technology," *Biotechniques,* vol. 11, pp. 620-&, Nov 1991.

[18] S. Lofas, M. Malmqvist, I. Ronnberg, E. Stenberg, B. Liedberg, and I. Lundstrom, "Bioanalysis with Surface-Plasmon Resonance," *Sensors and Actuators B-Chemical,* vol. 5, pp. 79-84, Aug-Dec 1991.

[19] M. A. Cooper, "Label-free screening of bio-molecular interactions," *Analytical and Bioanalytical Chemistry,* vol. 377, pp. 834-842, Nov 2003.

[20] S. K. Lee, S. G. Park, J. H. Moon, and S. M. Yang, "Holographic fabrication of photonic nanostructures for optofluidic integration," *Lab on a Chip,* vol. 8, pp. 388-391, 2008.

[21] H. Y. Zhu, I. M. White, J. D. Suter, and X. D. Fan, "Phage-based label-free biomolecule detection in an opto-fluidic ring resonator," *Biosensors & Bioelectronics,* vol. 24, pp. 461-466, Nov 15, 2008.

[22] C. J. Choi and B. T. Cunningham, "A 96-well microplate incorporating a replica molded microfluidic network integrated with photonic crystal biosensors for high throughput kinetic biomolecular interaction analysis," *Lab on a Chip,* vol. 7, pp. 550-556, 2007.

[23] R. Magnusson and S. S. Wang, "New Principle for Optical Filters," *Applied Physics Letters,* vol. 61, pp. 1022-1024, Aug 31, 1992.

[24] D. Rosenblatt, A. Sharon, and A. A. Friesem, "Resonant grating waveguide structures," *IEEE Journal of Quantum Electronics,* vol. 33, pp. 2038-2059, Nov 1997.

[25] C. J. Choi and B. T. Cunningham, "Single-step fabrication and characterization of photonic crystal biosensors with polymer microfluidic channels," *Lab on a Chip,* vol. 6, pp. 1373-1380, Oct 2006.

[26] P. Y. Li, L. Bo, J. Gerstenmaier, and B. T. Cunningham, "A new method for label-free imaging of biomolecular interactions," *Sensors and Actuators B-Chemical,* vol. 99, pp. 6-13, Apr 15, 2004.

[27] E. H. Conrad, *Heparin-Binding Proteins*. San Diego, CA: Academic Press, 1998.

[28] R. I. W. Osmond, W. C. Kett, S. E. Skett, and D. R. Coombe, "Protein-heparin interactions measured by BIAcore 2000 are affected by the method of heparin immobilization," *Analytical Biochemistry,* vol. 310, pp. 199-207, Nov 15, 2002.

[29] S. Zou, C. E. Magura, and W. L. Hurley, "Heparin-Binding Properties of Lactoferrin and Lysozyme," *Comparative Biochemistry and Physiology B-Biochemistry & Molecular Biology,* vol. 103, pp. 889-895, Dec 1992.

[30] W. Zhang, N. Ganesh, I. D. Block, and B. T. Cunningham, "High sensitivity photonic crystal biosensor incorporating nanorod structures for enhanced surface area," *Sensors and Actuators B-Chemical,* vol. 131, pp. 279-284, Apr 14, 2008.

[31] P. R. Edwards and R. J. Leatherbarrow, "Determination of association rate constants by an optical biosensor using initial rate analysis," *Analytical Biochemistry,* vol. 246, pp. 1-6, Mar 1, 1997.

[32] K. Maehashi, T. Katsura, K. Kerman, Y. Takamura, K. Matsumoto, and E. Tamiya, "Label-free protein biosensor based on aptamer-modified carbon

nanotube field-effect transistors," *Analytical Chemistry,* vol. 79, pp. 782-787, Jan 15, 2007.

[33] B. R. Baker, R. Y. Lai, M. S. Wood, E. H. Doctor, A. J. Heeger, and K. W. Plaxco, "An electronic, aptamer-based small-molecule sensor for the rapid, label-free detection of cocaine in adulterated samples and biological fluids," *Journal of the American Chemical Society,* vol. 128, pp. 3138-3139, Mar 15, 2006.

[34] M. F. Pineda, L. L. Y. Chan, T. Kuhlenschmidt, C. J. Choi, M. Kuhlenschmidt, and B. T. Cunningham, "Rapid Specific and Label-Free Detection of Porcine Rotavirus Using Photonic Crystal Biosensors," *IEEE Sensors Journal,* vol. 9, pp. 470-477, Apr 2009.

[35] R. Maalouf, C. Fournier-Wirth, J. Coste, H. Chebib, Y. Saikali, O. Vittori, A. Errachid, J. P. Cloarec, C. Martelet, and N. Jaffrezic-Renault, "Label-free detection of bacteria by electrochemical impedance spectroscopy: Comparison to surface plasmon resonance," *Analytical Chemistry,* vol. 79, pp. 4879-4886, Jul 1, 2007.

[36] L. L. Chan, S. L. Gosangari, K. L. Watkin, and B. T. Cunningham, "Label-free imaging of cancer cells using photonic crystal biosensors and application to cytotoxicity screening of a natural compound library," *Sensors and Actuators B-Chemical,* vol. 132, pp. 418-425, Jun 16, 2008.

[37] R. L. Rich and D. G. Myszka, "Higher-throughput, label-free, real-time molecular interaction analysis," *Analytical Biochemistry,* vol. 361, pp. 1-6, Feb 1, 2007.

[38] A. D. Taylor, J. Ladd, Q. M. Yu, S. F. Chen, J. Homola, and S. Y. Jiang, "Quantitative and simultaneous detection of four foodborne bacterial pathogens with a multi-channel SPR sensor," *Biosensors & Bioelectronics,* vol. 22, pp. 752-758, Dec 15, 2006.

[39] C. Barzen, A. Brecht, and G. Gauglitz, "Optical multiple-analyte immunosensor for water pollution control," *Biosensors & Bioelectronics,* vol. 17, pp. 289-295, Apr 2002.

[40] R. W. Glaser, "Antigen-Antibody Binding and Mass-Transport by Convection and Diffusion to a Surface - a 2-Dimensional Computer-Model of Binding and Dissociation Kinetics," *Analytical Biochemistry,* vol. 213, pp. 152-161, Aug 15, 1993.

[41] P. Schuck and A. P. Minton, "Analysis of mass transport-limited binding kinetics in evanescent wave biosensors," *Analytical Biochemistry,* vol. 240, pp. 262-272, Sep 5, 1996.

[42] G. J. Ciambrone, V. F. Liu, D. C. Lin, R. P. McGuinness, G. K. Leung, and S. Pitchford, "Cellular dielectric spectroscopy: A powerful new approach to label-free cellular analysis," *Journal of Biomolecular Screening,* vol. 9, pp. 467-480, Sep 2004.

[43] A. M. Armani, R. P. Kulkarni, S. E. Fraser, R. C. Flagan, and K. J. Vahala, "Label-free, single-molecule detection with optical microcavities," *Science,* vol. 317, pp. 783-787, Aug 10, 2007.

[44] F. Vollmer and S. Arnold, "Whispering-gallery-mode biosensing: label-free detection down to single molecules," *Nature Methods,* vol. 5, pp. 591-596, Jul 2008.

[45] D. Wassaf, G. N. Kuang, K. Kopacz, Q. L. Wu, Q. Nguyen, M. Toews, J. Cosic, J. Jacques, S. Wiltshire, J. Lambert, C. C. Pazmany, S. Hogan, R. C. Ladner, A. E. Nixon, and D. J. Sexton, "High-throughput affinity ranking of antibodies using surface plasmon resonance microarrays," *Analytical Biochemistry,* vol. 351, pp. 241-253, Apr 15, 2006.

[46] E. Ozkumur, J. W. Needham, D. A. Bergstein, R. Gonzalez, M. Cabodi, J. M. Gershoni, B. B. Goldberg, and M. S. Unlu, "Label-free and dynamic detection of biomolecular interactions for high-throughput microarray applications," *Proceedings of the National Academy of Sciences of the United States of America,* vol. 105, pp. 7988-7992, Jun 10, 2008.

[47] M. Zhao, X. F. Wang, and D. D. Nolte, "Molecular interferometric imaging," *Optics Express,* vol. 16, pp. 7102-7118, May 12, 2008.

[48] R. L. Rich, M. J. Cannon, J. Jenkins, P. Pandian, S. Sundaram, R. Magyar, J. Brockman, J. Lambert, and D. G. Myszka, "Extracting kinetic rate constants from surface plasmon resonance array systems," *Analytical Biochemistry,* vol. 373, pp. 112-120, Feb 1, 2008.

[49] R. McKendry, J. Y. Zhang, Y. Arntz, T. Strunz, M. Hegner, H. P. Lang, M. K. Baller, U. Certa, E. Meyer, H. J. Guntherodt, and C. Gerber, "Multiple label-free biodetection and quantitative DNA-binding assays on a nanomechanical cantilever array," *Proceedings of the National Academy of Sciences of the United States of America,* vol. 99, pp. 9783-9788, Jul 23, 2002.

[50] Z. Q. Gao, A. Agarwal, A. D. Trigg, N. Singh, C. Fang, C. H. Tung, Y. Fan, K. D. Buddharaju, and J. M. Kong, "Silicon nanowire arrays for label-free detection of DNA," *Analytical Chemistry,* vol. 79, pp. 3291-3297, May 1, 2007.

[51] A. L. Washburn, L. C. Gunn, and R. C. Bailey, "Label-Free Quantitation of a Cancer Biomarker in Complex Media Using Silicon Photonic Microring Resonators," *Analytical Chemistry,* vol. 81, pp. 9499-9506, Nov 15, 2009.

[52] S. Mandal and D. Erickson, "Nanoscale optofluidic sensor arrays," *Optics Express,* vol. 16, pp. 1623-1631, Feb 4, 2008.

[53] I. Barbulovic-Nad, M. Lucente, Y. Sun, M. J. Zhang, A. R. Wheeler, and M. Bussmann, "Bio-microarray fabrication techniques - A review," *Critical Reviews in Biotechnology,* vol. 26, pp. 237-259, Oct-Dec 2006.

[54] B. R. Schudel, C. J. Choi, B. T. Cunningham, and P. J. A. Kenis, "Microfluidic chip for combinatorial mixing and screening of assays," *Lab on a Chip,* vol. 9, pp. 1676-1680, 2009.

[55] L. L. Chan, B. T. Cunningham, P. Y. Li, and D. Puff, "A self-referencing method for microplate label-free photonic-crystal biosensors," *IEEE Sensors Journal,* vol. 6, pp. 1551-1556, Dec 2006.

[56] C. J. Choi, I. D. Block, B. Bole, D. Dralle, and B. T. Cunningham, "Label-Free Photonic Crystal Biosensor Integrated Microfluidic Chip for Determination of Kinetic Reaction Rate Constants," *IEEE Sensors Journal,* vol. 9, pp. 1697-1704, Dec 2009.

[57] Y. Liu, W. Zhang, X. Yu, H. W. Zhang, R. Zhao, D. Shangguan, Y. Li, B. F. Shen, and G. Q. Liu, "Quartz crystal biosensor for real-time kinetic analysis of interaction between human TNF-alpha and monoclonal antibodies," *Sensors and Actuators B-Chemical,* vol. 99, pp. 416-424, May 1, 2004.

[58] P. S. Dittrich and A. Manz, "Lab-on-a-chip: microfluidics in drug discovery," *Nat Rev Drug Discov,* vol. 5, pp. 210-218, 2006.
[59] V. Elisabeth, "Microfluidic chips for clinical and forensic analysis," *Electrophoresis,* vol. 23, pp. 677-712, 2002.
[60] T. H. Schulte, R. L. Bardell, and B. H. Weigl, "Microfluidic technologies in clinical diagnostics," *Clinica Chimica Acta,* vol. 321, pp. 1-10, 2002.
[61] J. F. Zhong, Y. Chen, J. S. Marcus, A. Scherer, S. R. Quake, C. R. Taylor, and L. P. Weiner, "A microfluidic processor for gene expression profiling of single human embryonic stem cells," *Lab on a Chip,* vol. 8, pp. 68-74, 2008.
[62] E. Garcia-Egido, V. Spikmans, S. Y. F. Wong, and B. H. Warrington, "Synthesis and analysis of combinatorial libraries performed in an automated micro reactor system," *Lab on a Chip,* vol. 3, pp. 73-76, 2003.
[63] T. Hatakeyama, D. L. L. Chen, and R. F. Ismagilov, "Microgram-scale testing of reaction conditions in solution using nanoliter plugs in microfluidics with detection by MALDI-MS," *Journal of the American Chemical Society,* vol. 128, pp. 2518-2519, Mar 1, 2006.
[64] R. F. Ismagilov, J. M. K. Ng, P. J. A. Kenis, and G. M. Whitesides, "Microfluidic arrays of fluid-fluid diffusional contacts as detection elements and combinatorial tools," *Analytical Chemistry,* vol. 73, pp. 5207-5213, Nov 1, 2001.
[65] I. D. Block, L. L. Chan, and B. T. Cunningham, "Photonic crystal optical biosensor incorporating structured low-index porous dielectric," *Sensors and Actuators B-Chemical,* vol. 120, pp. 187-193, Dec 14, 2006.
[66] L. L. Chan, B. T. Cunningham, P. Y. Li, and D. Puff, "Self-referenced assay method for photonic crystal biosensors: Application to small molecule analytes," *Sensors and Actuators B-Chemical,* vol. 120, pp. 392-398, Jan 10, 2007.
[67] C. C. Lee, G. D. Sui, A. Elizarov, C. Y. J. Shu, Y. S. Shin, A. N. Dooley, J. Huang, A. Daridon, P. Wyatt, D. Stout, H. C. Kolb, O. N. Witte, N. Satyamurthy, J. R. Heath, M. E. Phelps, S. R. Quake, and H. R. Tseng, "Multistep synthesis of a radiolabeled imaging probe using integrated microfluidics," *Science,* vol. 310, pp. 1793-1796, Dec 16, 2005.
[68] M. A. Unger, H. P. Chou, T. Thorsen, A. Scherer, and S. R. Quake, "Monolithic microfabricated valves and pumps by multilayer soft lithography," *Science,* vol. 288, pp. 113-116, Apr 7, 2000.
[69] C. L. Hansen, E. Skordalakes, J. M. Berger, and S. R. Quake, "A robust and scalable microfluidic metering method that allows protein crystal growth by free interface diffusion," *Proceedings of the National Academy of Sciences of the United States of America,* vol. 99, pp. 16531-16536, Dec 24, 2002.
[70] W. H. Grover, A. M. Skelley, C. N. Liu, E. T. Lagally, and R. A. Mathies, "Monolithic membrane valves and diaphragm pumps for practical large-scale integration into glass microfluidic devices," *Sensors and Actuators B-Chemical,* vol. 89, pp. 315-323, Apr 1, 2003.
[71] W. H. Grover, R. H. C. Ivester, E. C. Jensen, and R. A. Mathies, "Development and multiplexed control of latching pneumatic valves using microfluidic logical structures," *Lab on a Chip,* vol. 6, pp. 623-631, 2006.
[72] D. S. Grubisha, R. J. Lipert, H. Y. Park, J. Driskell, and M. D. Porter, "Femtomolar detection of prostate-specific antigen: An immunoassay based on

surface-enhanced Raman scattering and immunogold labels," *Analytical Chemistry*, vol. 75, pp. 5936-5943, Nov 1, 2003.

[73] Y. W. C. Cao, R. C. Jin, and C. A. Mirkin, "Nanoparticles with Raman spectroscopic fingerprints for DNA and RNA detection," *Science*, vol. 297, pp. 1536-1540, Aug 30, 2002.

[74] O. Neumann, D. M. Zhang, F. Tam, S. Lal, P. Wittung-Stafshede, and N. J. Halas, "Direct Optical Detection of Aptamer Conformational Changes Induced by Target Molecules," *Analytical Chemistry*, vol. 81, pp. 10002-10006, Dec 15, 2009.

[75] S. Shanmukh, L. Jones, J. Driskell, Y. P. Zhao, R. Dluhy, and R. A. Tripp, "Rapid and sensitive detection of respiratory virus molecular signatures using a silver nanorod array SERS substrate," *Nano Letters*, vol. 6, pp. 2630-2636, Nov 8, 2006.

[76] R. M. Jarvis and R. Goodacre, "Discrimination of bacteria using surface-enhanced Raman spectroscopy," *Analytical Chemistry*, vol. 76, pp. 40-47, Jan 1, 2004.

[77] O. M. Primera-Pedrozo, J. I. Jerez-Rozo, E. De la Cruz-Montoya, T. Luna-Pineda, L. C. Pacheco-Londono, and S. P. Hernandez-Rivera, "Nanotechnology-based detection of explosives and biological agents simulants," *IEEE Sensors Journal*, vol. 8, pp. 963-973, May-Jun 2008.

[78] M. Fleischmann, P. J. Hendra, and A. J. McQuillan, "Raman-Spectra of Pyridine Adsorbed at a Silver Electrode," *Chemical Physics Letters*, vol. 26, pp. 163-166, 1974.

[79] D. L. Jeanmaire and R. P. Vanduyne, "Surface Raman Spectroelectrochemistry .1. Heterocyclic, Aromatic, and Aliphatic-Amines Adsorbed on Anodized Silver Electrode," *Journal of Electroanalytical Chemistry*, vol. 84, pp. 1-20, 1977.

[80] C. L. Haynes, A. D. McFarland, and R. P. Van Duyne, "Surface-enhanced Raman spectroscopy," *Analytical Chemistry*, vol. 77, pp. 338A-346A, Sep 1, 2005.

[81] M. Moskovits, "Surface-Enhanced Spectroscopy," *Reviews of Modern Physics*, vol. 57, pp. 783-826, 1985.

[82] K. Kneipp, Y. Wang, H. Kneipp, L. T. Perelman, I. Itzkan, R. Dasari, and M. S. Feld, "Single molecule detection using surface-enhanced Raman scattering (SERS)," *Physical Review Letters*, vol. 78, pp. 1667-1670, Mar 3, 1997.

[83] S. M. Nie and S. R. Emory, "Probing single molecules and single nanoparticles by surface-enhanced Raman scattering," *Science*, vol. 275, pp. 1102-1106, Feb 21, 1997.

[84] Y. Lu, G. L. Liu, J. Kim, Y. X. Mejia, and L. P. Lee, "Nanophotonic crescent moon structures with sharp edge for ultrasensitive biomolecular detection by local electromagnetic field enhancement effect," *Nano Letters*, vol. 5, pp. 119-124, Jan 2005.

[85] P. G. Etchegoin and E. C. Le Ru, "A perspective on single molecule SERS: current status and future challenges," *Physical Chemistry Chemical Physics*, vol. 10, pp. 6079-6089, 2008.

[86] N. P. W. Pieczonka and R. F. Aroca, "Single molecule analysis by surfaced-enhanced Raman scattering," *Chemical Society Reviews*, vol. 37, pp. 946-954, 2008.

[87] P. F. Liao, J. G. Bergman, D. S. Chemla, A. Wokaun, J. Melngailis, A. M. Hawryluk, and N. P. Economou, "Surface-Enhanced Raman-Scattering from

Microlithographic Silver Particle Surfaces," *Chemical Physics Letters*, vol. 82, pp. 355-359, 1981.

[88] L. Gunnarsson, E. J. Bjerneld, H. Xu, S. Petronis, B. Kasemo, and M. Kall, "Interparticle coupling effects in nanofabricated substrates for surface-enhanced Raman scattering," *Applied Physics Letters*, vol. 78, pp. 802-804, Feb 5, 2001.

[89] N. Felidj, J. Aubard, G. Levi, J. R. Krenn, A. Hohenau, G. Schider, A. Leitner, and F. R. Aussenegg, "Optimized surface-enhanced Raman scattering on gold nanoparticle arrays," *Applied Physics Letters*, vol. 82, pp. 3095-3097, May 5, 2003.

[90] N. Felidj, S. L. Truong, J. Aubard, G. Levi, J. R. Krenn, A. Hohenau, A. Leitner, and F. R. Aussenegg, "Gold particle interaction in regular arrays probed by surface enhanced Raman scattering," *Journal of Chemical Physics*, vol. 120, pp. 7141-7146, Apr 15, 2004.

[91] A. Gopinath, S. V. Boriskina, W. R. Premasiri, L. Ziegler, B. M. Reinhard, and L. Dal Negro, "Plasmonic Nanogalaxies: Multiscale Aperiodic Arrays for Surface-Enhanced Raman Sensing," *Nano Letters*, vol. 9, pp. 3922-3929, Nov 2009.

[92] G. L. Liu and L. P. Lee, "Nanowell surface enhanced Raman scattering arrays fabricated by soft-lithography for label-free biomolecular detections in integrated microfluidics," *Applied Physics Letters*, vol. 87, pp. 074101-074103, Aug 15, 2005.

[93] A. J. Baca, T. T. Truong, L. R. Cambrea, J. M. Montgomery, S. K. Gray, D. Abdula, T. R. Banks, J. M. Yao, R. G. Nuzzo, and J. A. Rogers, "Molded plasmonic crystals for detecting and spatially imaging surface bound species by surface-enhanced Raman scattering," *Applied Physics Letters*, vol. 94, pp. 243109-243111, Jun 15, 2009.

[94] K. D. Alexander, M. J. Hampton, S. P. Zhang, A. Dhawan, H. X. Xu, and R. Lopez, "A high-throughput method for controlled hot-spot fabrication in SERS-active gold nanoparticle dimer arrays," *Journal of Raman Spectroscopy*, vol. 40, pp. 2171-2175, Dec 2009.

[95] C. L. Haynes and R. P. Van Duyne, "Nanosphere lithography: A versatile nanofabrication tool for studies of size-dependent nanoparticle optics," *Journal of Physical Chemistry B*, vol. 105, pp. 5599-5611, Jun 21, 2001.

[96] L. A. Dick, A. D. McFarland, C. L. Haynes, and R. P. Van Duyne, "Metal film over nanosphere (MFON) electrodes for surface-enhanced Raman spectroscopy (SERS): Improvements in surface nanostructure stability and suppression of irreversible loss," *Journal of Physical Chemistry B*, vol. 106, pp. 853-860, Jan 31, 2002.

[97] A. J. Haes, C. L. Haynes, A. D. McFarland, G. C. Schatz, R. R. Van Duyne, and S. L. Zou, "Plasmonic materials for surface-enhanced sensing and spectroscopy," *MRS Bulletin*, vol. 30, pp. 368-375, May 2005.

[98] K. B. Biggs, J. P. Camden, J. N. Anker, and R. P. Van Duyne, "Surface-Enhanced Raman Spectroscopy of Benzenethiol Adsorbed from the Gas Phase onto Silver Film over Nanosphere Surfaces: Determination of the Sticking Probability and Detection Limit Time," *Journal of Physical Chemistry A*, vol. 113, pp. 4581-4586, Apr 23, 2009.

[99] I. D. Block, P. C. Mathias, N. Ganesh, S. I. Jones, B. R. Dorvel, V. Chaudhery, L. O. Vodkin, R. Bashir, and B. T. Cunningham, "A detection instrument for enhanced-fluorescence and label-free imaging on photonic crystal surfaces," *Optics Express,* vol. 17, pp. 13222-13235, Jul 20, 2009.

[100] N. Ganesh, W. Zhang, P. C. Mathias, E. Chow, J. A. N. T. Soares, V. Malyarchuk, A. D. Smith, and B. T. Cunningham, "Enhanced fluorescence emission from quantum dots on a photonic crystal surface," *Nature Nanotechnology,* vol. 2, pp. 515-520, Aug 2007.

[101] W. Zhang, N. Ganesh, P. C. Mathias, and B. T. Cunningham, "Enhanced Fluorescence on a Photonic Crystal Surface Incorporating Nanorod Structures," *Small,* vol. 4, pp. 2199-2203, Dec 2008.

[102] M. Lu, S. Choi, C. J. Wagner, J. G. Eden, and B. T. Cunningham, "Label free biosensor incorporating a replica-molded, vertically emitting distributed feedback laser," *Applied Physics Letters,* vol. 92, pp. 261502-261504, Jun 30, 2008.

[103] F. Y. Yang, G. Yen, G. Rasigade, J. A. N. T. Soares, and B. T. Cunningham, "Optically tuned resonant optical reflectance filter," *Applied Physics Letters,* vol. 92, pp. 091115-091117, Mar 3, 2008.

[104] G. J. Slavik, G. Ragetly, N. Ganesh, D. J. Griffon, and B. T. Cunningham, "A replica molding technique for producing fibrous chitosan scaffolds for cartilage engineering," *Journal of Materials Chemistry,* vol. 17, pp. 4095-4101, 2007.

[105] M. Lu, S. J. Park, B. T. Cunningham, and J. G. Eden, "Microcavity plasma devices and arrays fabricated by plastic-based replica molding," *Journal of Microelectromechanical Systems,* vol. 16, pp. 1397-1402, Dec 2007.

[106] A. Campion and P. Kambhampati, "Surface-enhanced Raman scattering," *Chemical Society Reviews,* vol. 27, pp. 241-250, Jul 1998.

[107] Y. P. Zhao, S. B. Chaney, S. Shanmukh, and R. A. Dluhy, "Polarized surface enhanced raman and absorbance spectra of aligned silver nanorod arrays," *Journal of Physical Chemistry B,* vol. 110, pp. 3153-3157, Feb 23, 2006.

[108] P. L. Stiles, J. A. Dieringer, N. C. Shah, and R. R. Van Duyne, "Surface-Enhanced Raman Spectroscopy," *Annual Review of Analytical Chemistry,* vol. 1, pp. 601-626, 2008.

[109] "National Kidney Foundation: The Facts About Chronic Kidney Disease (CKD)," *Kidney Disease*, National Kidney Foundation, 2008.

[110] B. Schiller and J. Moran, "Dialysis while you sleep - an alternative therapy," *At Home with AAKP,* American Association of Kidney Patients, 2009.

[111] I. Hatcher, M. Sullivan, J. Hutchinson, S. Thurman, and F. A. Gaffney, "An intravenous medication safety system - Preventing high-risk medication errors at the point of care," *Journal of Nursing Administration,* vol. 34, pp. 437-439, Oct 2004.

[112] S. Thurman, M. Sullivan, M. A. Williams, and A. Gaffney, "Intravenous medication safety systems help prevent harm and career-ending mistakes," *Journal of Nursing Administration,* vol. 34, pp. 2-4, Dec 2004.

[113] K. Wilson and M. Sullivan, "Preventing medication errors with smart infusion technology," *American Journal of Health-System Pharmacy,* vol. 61, pp. 177-183, Jan 15, 2004.

[114] D. P. Phillips, N. Christenfeld, and L. M. Glynn, "Increase in US medication-error deaths between 1983 and 1993," *Lancet,* vol. 351, pp. 643-644, Feb 28, 1998.
[115] S. K. Steingass, "Beyond pumps: Smarter infusion systems," *Journal of Nursing Administration,* vol. 34, pp. 10-10, Oct 2004.
[116] "U.S. Food and Drug Administration: Information for Healthcare Professionals - Intravenous Promethazine and Severe Tissue Injury, Including Gangrene," in *Postmarket Drug Safety Information for Patients and Providers*, U.S. Food and Drug Administration, 2009.
[117] W. R. Premasiri, R. H. Clarke, and M. E. Womble, "Urine analysis by laser Raman spectroscopy," *Lasers in Surgery and Medicine,* vol. 28, pp. 330-334, 2001.
[118] A. Radomska, R. Koncki, K. Pyrzynska, and S. Glab, "Bioanalytical system for control of hemodialysis treatment based on potentiometric biosensors for urea and creatinine," *Analytica Chimica Acta,* vol. 523, pp. 193-200, Oct 11, 2004.
[119] B. Premanode and C. Toumazou, "A novel, low power biosensor for real time monitoring of creatinine and urea in peritoneal dialysis," *Sensors and Actuators B-Chemical,* vol. 120, pp. 732-735, Jan 10, 2007.
[120] Y. Morishita, K. Nakane, T. Fukatsu, N. Nakashima, K. Tsuji, Y. Soya, K. Yoneda, S. Asano, and Y. Kawamura, "Kinetic assay of serum and urine for urea with use of urease and leucine dehydrogenase," *Clinical Chemistry,* vol. 43, pp. 1932-1936, Oct 1997.
[121] I. Basu, R. V. Subramanian, A. Mathew, A. M. Kayastha, A. Chadha, and E. Bhattacharya, "Solid state potentiometric sensor for the estimation of tributyrin and urea," *Sensors and Actuators B-Chemical,* vol. 107, pp. 418-423, May 27, 2005.
[122] J. V. de Melo, S. Cosnier, C. Mousty, C. Martelet, and N. Jaffrezic-Renault, "Urea biosensors based on immobilization of urease into two oppositely charged clays (Laponite and Zn-Al layered double hydroxides)," *Analytical Chemistry,* vol. 74, pp. 4037-4043, Aug 15, 2002.
[123] A. S. Jdanova, S. Poyard, A. P. Soldatkin, N. JaffrezicRenault, and C. Martelet, "Conductometric urea sensor. Use of additional membranes for the improvement of its analytical characteristics," *Analytica Chimica Acta,* vol. 321, pp. 35-40, Mar 8, 1996.
[124] A. Sansubrino and M. Mascini, "Development of an Optical-Fiber Sensor for Ammonia, Urea, Urease and Igg," *Biosensors & Bioelectronics,* vol. 9, pp. 207-216, 1994.
[125] W. Sant, M. L. Pourciel, J. Launay, T. Do Conto, A. Martinez, and P. Temple-Boyer, "Development of chemical field effect transistors for the detection of urea," *Sensors and Actuators B-Chemical,* vol. 95, pp. 309-314, Oct 15, 2003.
[126] A. Senillou, N. Jaffrezic-Renault, C. Martelet, and S. Cosnier, "A miniaturized urea sensor based on the integration of both ammonium based urea enzyme field effect transistor and a reference field effect transistor in a single chip," *Talanta,* vol. 50, pp. 219-226, Aug 23, 1999.
[127] R. A. Shaw, S. Kotowich, H. H. Mantsch, and M. Leroux, "Quantitation of protein, creatinine, and urea in urine by near-infrared spectroscopy," *Clinical Biochemistry,* vol. 29, pp. 11-19, Feb 1996.

[128] K. R. Ackermann, T. Henkel, and J. Popp, "Quantitative online detection of low-concentrated drugs via a SERS microfluidic system," *Chemphyschem*, vol. 8, pp. 2665-2670, Dec 20, 2007.